AD-A035 772   ROCKWELL INTERNATIONAL THOUSAND OAKS CALIF SCIENCE --ETC F/G 17/5
1.06 MICRON PHOTODETECTOR DEVELOPMENT.(U)
OCT 76 J S HARRIS, R C EDEN, L O BUBULAC   F33615-76-C-1001
UNCLASSIFIED   AFAL-TR-76-121   NL

1 OF 1
ADA035772

END
DATE
FILMED
3-77

ADA035772

AFAL-TR-76-121

1.06 MICRON PHOTODETECTOR DEVELOPMENT

SCIENCE CENTER, ROCKWELL INTERNATIONAL
1049 CAMINO DOS RIOS
THOUSAND OAKS, CALIFORNIA 91360

OCTOBER 1976

DDC
FEB 18 1977
RECEIVED
A

TECHNICAL REPORT AFAL-TR-76-121
FINAL REPORT 1 AUGUST 1975 - 1 FEBRUARY 1976

Approved for public release; distribution unlimited

AIR FORCE AVIONICS LABORATORY
AIR FORCE WRIGHT AERONAUTICAL LABORATORIES
AIR FORCE SYSTEMS COMMAND
WRIGHT-PATTERSON AIR FORCE BASE, OHIO 45433

NOTICE

When Government drawings, specifications, or other data are used for any purpose other than in connection with a definitely related Government procurement operation, the United States Government thereby incurs no responsibility nor any obligation whatsoever; and the fact that the government may have formulated, furnished, or in any way supplied the said drawings, specifications, or other data, is not to be regarded by implication or otherwise as in any manner licensing the holder or any other person or corporation, or conveying any rights or permission to manufacture, use, or sell any patented invention that may in any way be related thereto.

This report has been reviewed by the Information Office (OI) and is releasable to the National Technical Information Service (NTIS). At NTIS, it will be available to the general public, including foreign nations.

This technical report has been reviewed and is approved for publication.

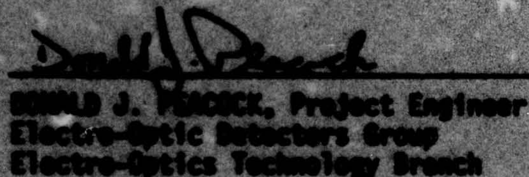

DONALD J. PEACOCK, Project Engineer
Electro-Optic Detectors Group
Electro-Optics Technology Branch

FOR THE COMMANDER

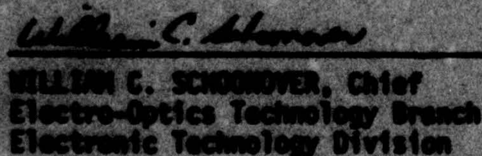

WILLIAM C. SCHOONOVER, Chief
Electro-Optics Technology Branch
Electronic Technology Division

Copies of this report should not be returned unless return is required by security considerations, contractual obligations, or notice on a specific document.

AIR FORCE - 20 DECEMBER 76 - 100

UNCLASSIFIED

SECURITY CLASSIFICATION OF THIS PAGE (When Data Entered)

REPORT DOCUMENTATION PAGE

READ INSTRUCTIONS BEFORE COMPLETING FORM

1. REPORT NUMBER: AFAL-TR-76-121	2. GOVT ACCESSION NO. / 3. RECIPIENT'S CATALOG NUMBER
4. TITLE (and Subtitle): 1.06 MICRON PHOTODETECTOR DEVELOPMENT.	5. TYPE OF REPORT & PERIOD COVERED: FINAL REPORT, 1 August 1975 through 1 February 1976
	6. PERFORMING ORG. REPORT NUMBER
7. AUTHOR(s): J. S. Harris, Jr., R. C. Eden, L. O. Bubulac, I. Deyhimy, K. Nakano and J. R. Waldrop	8. CONTRACT OR GRANT NUMBER(s): F33615-76-C-1001
9. PERFORMING ORGANIZATION NAME AND ADDRESS: Science Center, Rockwell International, 1049 Camino Dos Rios, Thousand Oaks, CA 91360	10. PROGRAM ELEMENT, PROJECT, TASK AREA & WORK UNIT NUMBERS: 2001 02 04
11. CONTROLLING OFFICE NAME AND ADDRESS: Air Force Avionics Laboratory, Air Force Systems Command, Wright-Patterson Air Force Base, Ohio 45433	12. REPORT DATE: October 1976
	13. NUMBER OF PAGES
14. MONITORING AGENCY NAME & ADDRESS (if different from Controlling Office)	15. SECURITY CLASS. (of this report): UNCLASSIFIED
	15a. DECLASSIFICATION/DOWNGRADING SCHEDULE

16. DISTRIBUTION STATEMENT (of this Report)

Approved for public release; distribution unlimited.

17. DISTRIBUTION STATEMENT (of the abstract entered in Block 20, if different from Report)

18. SUPPLEMENTARY NOTES

19. KEY WORDS (Continue on reverse side if necessary and identify by block number)

1.06 Micron	Photodiode
Photodetector	Photocathode
Nd-YAG Laser	Heterojunctions
Optical Receiver	III-V Compounds

20. ABSTRACT (Continue on reverse side if necessary and identify by block number)

The design and progress towards realizing very high sensitivity 1.06μm photodetectors are reported. This research program consists of two projects: a high sensitivity 5 MHz optical receiver and a field-assisted double heterojunction photocathode. A 5 MHz, 1.06μm GaAsSb avalanche photodiode (APD) receiver was built, tested and its noise performance modeled to determine the ultimate performance achievable with this technology. The initial receiver was better than an equivalent Si APD receiver by a factor of 2, and this was

DD FORM 1 JAN 73 1473 EDITION OF 1 NOV 65 IS OBSOLETE

UNCLASSIFIED

SECURITY CLASSIFICATION OF THIS PAGE (When Data Entered)

389949

with very low gain in the GaAsSb APD. Considerable overall improvement is predicted with higher gain APDs. Cs activation to achieve negative electron affinity (NEA) on heterojunction devices has been the major emphasis in the photocathode project. A sputter cleaning and annealing process was developed which produced excellent activations on GaAs. The first results are reported on a double heterojunction device which has been activated to NEA and operated in vacuum. This device exhibited very large dark current under applied bias which is not yet understood. Further work in understanding this dark current will be required in order to realize the potential of the field-assisted photocathode.

FOREWORD

This report was prepared by the Science Center, Rockwell International under Contract F33615-76-C-1001, Project No. 2001, Task Area No. 002 and Work Unit No. A004. This report covers the period 1 August 1975 through 1 February 1976 and is the Final Report on this contract. The work described herein was carried out Science Center, Rockwell International, Thousand Oaks, California.

The project engineers were Drs. J. S. Harris, Jr. and Dr. R. C. Eden. The program manager was Dr. A. S. Joseph.

The submittal date of this report was April 1976.

The Air Force project engineer is Donald J. Peacock, AFAL/DHO-3.

ACCESSION for
NTIS White Section
DDC Buff Section
UNANNOUNCED
JUSTIFICATION
BY
DISTRIBUTION/AVAILABILITY CODES
Dist. AVAIL. and/or SPECIAL
A

TABLE OF CONTENTS

		Page
1.0	INTRODUCTION	1
2.0	PROGRAM APPROACH AND GOALS	3
3.0	RESULTS	6
3.1	1.06μm APD Receiver	
3.1.1	Growth of $Al_xGa_{1-x}Sb$ for 1.06μm Avalanche Photodiodes	7
3.1.2	AlGaSb Avalanche Photodiode Fabrication	14
3.1.3	GaAlSb Avalanche Photodiode Measurements	14
3.1.4	5 MHz APD Receiver Model	20
3.1.5	5 MHz APD Receiver Measurements	29
3.2	Double Heterojunction Photocathode	47
3.2.1	Device Processing	53
3.2.2	Cs Activation	57
3.2.2.1	Effect of Cs and O_2 on Photoyield	57
3.2.2.2	Sputter Cleaning Experiments	60
3.2.2.3	Cold Cathode Activation	71
3.2.2.4	Double Heterojunction Photocathode Activation ..	78
4.0	CONCLUSIONS AND RECOMMENDATIONS	82
5.0	REFERENCES	84

LIST OF ILLUSTRATIONS

Figure		Page
2.1	The proposed new device structure in which the epitaxial structure is eutectically bonded, absorber down, to a second GaAs substrate. The original GaAs growth substrate is then selectively removed by a combination of lapping and chemical and electrolytic etching to expose the emitter surface.	4
3.1	Experimental 500°C solidus line for GaAlSb showing solid composition vs. Al composition in the liquid.	8
3.2	Experimental 500°C liquidus line for GaAlSb showing melt composition vs. mole fraction of Al in the liquid.	9
3.3	Energy band structure vs. composition for GaAlSb.	10
3.4	GaAlSb lattice matched avalanche photodiode structure.	12
3.5	Relative quantum efficiency vs. wavelength of GaAlSb photodiode.	17
3.6	Doping profile carrier concentration vs. depletion width of GaAlSb photodiode.	18
3.7	Scanning Electron Microscope induce current mode photomicrograph of GaAlSb photodiode.	19
3.8	Scanning Light Microscope intensity modulated photomicrograph of GaAlSb photodiode response to 1.06μm laser.	21
3.9	5 MHz receiver block diagram arrangement of component parts of receiver.	22

LIST OF ILLUSTRATIONS (Con't)

Figure		Page
3.10	Model used for analysis of signal and noise response. e_1 is the equivalent input noise voltage generator of the preamp, e_2 is the Johnson noise voltage generator of the conductance G_F. In (b), G_I replaces the input conductance of the preamp and the conductance of the APD and i_{nj} replaces e_2.	24
3.11	Outputs of nosie analysis computer program. (a) real and imaginary parts of transimpedance. (b) sum of squares of real and imaginary parts of transimpedance; $(\text{magnitude})^2$ of frequency response and output noise voltage vs. frequency.	28
3.12	Experimental configuration for measurement of open loop gain-phase.	30
3.13	(a) 8 cycles of two sine waves of equal frequency. One since wave totally buried in noise. (b) Cross-correlation of the two sine waves in (a).	32
3.14	(a) Test capacitor for measuring impulse response and (b) its calibration.	33
3.15	(a) Noise output and its statistical distribution. (b) Measured statistical distribution of output noise, its log superimposed with log of a Gaussian distribution.	35
3.16	Measured amplitude vs. frequency response for receiver #3 as determined by taking FFT of the impulse response. (a) Direct output of the DPO on linear axes and (b) corrected to logarithmic axes.	39
3.17	Circuit model showing peaking in the passband.	40

LIST OF ILLUSTRATIONS (Con't)

Figure		Page
3.18	Magnitude of transimpedance of Receiver #3 vs. frequency.	41
3.19	Comparison of measured output noise voltage spectral density vs. frequency with various predictions of noise model for receiver #3.	44
3.20	Comaprison of measured output noise voltage spectral density vs. frequency with various predictions of noise model for receiver #1.	46
3.21	Energy band diagram for the 1.06μm heterojunction photocathode assuming graded junctions with no "abrupt discontinuities." (a) the p-n-p device at zero bias. (b) the p-n-p device biased to "punch through" under operating conditions showing no barrier in the conduction band and ~ 0.4 eV barrier in the valence band.	50
3.22	Schematic diagram of the double heterojunction photo-cathode structure for activation. The thickness, chemical composition, dopant and carrier concentration for each layer is also shown in the diagram.	52
3.23	Schematic diagram of the double heterojunction photo-cathode showing the planned mounting, bonding and substrate removal required to produce a device for Cs activation.	54
3.24	The proposed new device structure in which the epitaxial structure is eutectically bonded, absorber down, to a second GaAs substrate. The original GaAs growth substrate is then selectively removed by a combination of lapping and chemical and electrolytic etching to expose the emitter surface.	56

LIST OF ILLUSTRATIONS (Con't)

Figure		Page
3.25	Influence of Cs - 0 cycles on spectral yield; (a) Cs only; (b) 1 cycle; (c) 2 cycles; (d) 3 cycles; (e) 10 cycles.	59
3.26	Data in Figure 3.25 replotted as $\frac{1-R}{Y}$ vs. $\frac{1}{\alpha}$.	
3.27	Comparison of spectral yield before and after sputter cleaning with 1 keV Ar^+ ions and 590°C anneal temperature.	63
3.28	Spectral yield before sputter for high-sensitivity sample (1005µ amps/1µmen).	64
3.29	$\frac{1-R}{Y}$ vs. $\frac{1}{\alpha}$ plot for Figure 3.28 data. $p = 25\%$, $L = 8\mu m$.	65
3.30	Spectral yield after sputter cleaning for sample in Figure 3.28 sputtered with 250 keV Ar^+ ions, followed by 605°C anneal.	66
3.31	$\frac{1-R}{Y}$ vs. $\frac{1}{\alpha}$ plot for Figure 3.30 data. $p = 17\%$, $L = 8\mu m$.	67
3.32	Auger electron spectra before sputtering; (a) initial, before heat cleaning; (b) after heat clean, 2 min at 590°C; (c) after Cs - 0 activation.	69
3.33	Auger electron spectra after sputtering: (a) initial, before sputtering; (b) after 1 hr. sputter with 250 eV Ar^+ ions, (c) after 30 min. anneal at 605°C; (d) after Cs - 0 activation.	70
3.34	Schematic view of GaAs-GaAlAs heterojunction cold-cathode structure.	72
3.35	Log I vs. V plots for a cold cathode sample mounted in the activation chamber before any processing.	73

LIST OF ILLUSTRATIONS (Con't)

Figure		Page
3.36	Log I vs. V plots for the same cold cathode sample after heat cleaning for 2 min. at 610°C.	74
3.37	Log I vs. V plots for the cold cathode sample after Cs and O_2 activation to reach NEA.	75
3.38	Log I vs. V plots for the same cold cathode sample after allowing the sample to sit in the chamber for 24 hours (solid lines) and then after a second Cs and O_2 activation to achieve good photoemission (dashed lines).	76
3.39	Current vs. voltage characteristic for the double heterojunction photocathode. (a) Before and after cesiation, (remains identical) the 2 curves are in the dark and with white light on the emitter surface showing good collection of photoelectrons at the emitter-hole barrier junction. (b) After excess cesiation, the device becomes shorted.	80

1.0 INTRODUCTION

Laser systems utilizing the 1.06μm Nd:YAG laser are of vital importance to the Air Force. Major applications include high data rate satellite communications, laser-illuminated imaging, laser tracking, laser range finding and target designation. In all of these applications, the optical detector (photodiode or photocathode) plays a crucial role in determining the overall system performance. Recognizing that the Si avalanche photodiode and S-1 photocathode were completely inadequate for the above systems, the Air Force Avionics Laboratory initiated a research program at the Science Center in 1971 to develop III-V alloy avalanche photodiodes and field-assisted photocathodes. The goal of this program was to develop improved 1.06μm optical detectors for future Air Force Systems.

The avalanche photodiode (APD) program was initially directed towards development of a 1 GHz photodiode for optical communications. This work clearly demonstrated that it is absolutely essential to develop an optical receiver as a coherent unit rather than separate efforts on APD's and low noise preamplifiers. This approach to total receiver design has been very successful in developing a 1 GHz receiver and is being expanded into new areas. In this program we are addressing a new application, a laser-illuminated night imaging system. This system requires an optical receiver with video bandwidth (typically 5 MHz) and very high sensitivity. In this program, we successfully fabricated a 5 MHz receiver which was more sensitive by a factor of 2 in a 1 MHz bandwidth than an equivalent Si APD receiver. A noise model was developed for this receiver and based upon this model, considerably better performance can still be expected by optimizing our present approach to the 5 MHz receiver.

The field-assisted photocathode program has been directed toward the development of a new type of photocathode to yield a 20% efficient,

1.06μm device. In prior programs, the physical concepts for this device were demonstrated with internal photoemission measurements on a test structure. In this program, the entire emphasis has been on developing a Cs activation technique which maintains the heterojunction device integrity, developing a device processing technology compatible with Cs activation and demonstrating field-assisted photoemission into vacuum. State-of-the-art Cs activation on GaAs was achieved and a suitable sputter cleaning technique was developed. The first double heterojunction devices for activation were successfully fabricated and activated to negative electron affinity. Unexpectably large emitted dark current was observed with applied bias in our first measurements. Further work must be undertaken to understand the origin of this dark current as none was observed in the internal photoemission experiments.

Considerable progress has been made in both the photodiode and photocathode programs. Both efforts are largely dependent upon improvements in the emerging III-V alloys material technology. Because this is a young technology, a continuing research effort should yield impressive improvements in device performance. It is, however, essential to maintain such a research effort if the predicted performances are to be realized.

2.0 PROGRAM APPROACH AND GOALS

The 1.06μm photodetector development consists of two projects: an avalanche photodiode receiver project and a field assisted photocathode project.

The goal of the optical receiver effort is to develop a 1.06μm optical receiver with a 5 MHz bandwidth which can detect a modulated 1 nw laser signal with a minimum signal-to-noise ratio of 3. In order to reach this goal, it is necessary to improve the existing capability in both the avalanche photodiode and the preamplifier.

The approach to realize the above goal has been two fold. First, an effort has been initiated into new APD structures and materials which will increase the photodiode avalanche gain while still maintaining the low capacitance, high quantum efficiency and high speed of our existing devices. Second, a low input capacitance, transimpedance type of preamplifier has been designed, fabricated, and tested with existing APD structures. The noise performance of this present receiver is characterized and modeled to provide a sound basis for predicting the ultimate receiver performance with improved avalanche photodiodes.

The goal of the photocathode effort is to develop a high performance room temperature photocathode with 20% external quantum efficiency at 1.06μm and with a long lifetime. In order to achieve this goal, we designed a double heterojunction field assisted photocathode and have demonstrated that the device has the potential to reach the above goal.[1] The specific goal of the present effort is to demonstrate the entire device operation with photoemission into vacuum.

As described in our last report,[2] the photocathode structure can only be grown with the absorber layer last which complicates the device processing. The first structure which we attempted for device fabrication proved to be to fragile to withstand the thermal treatments

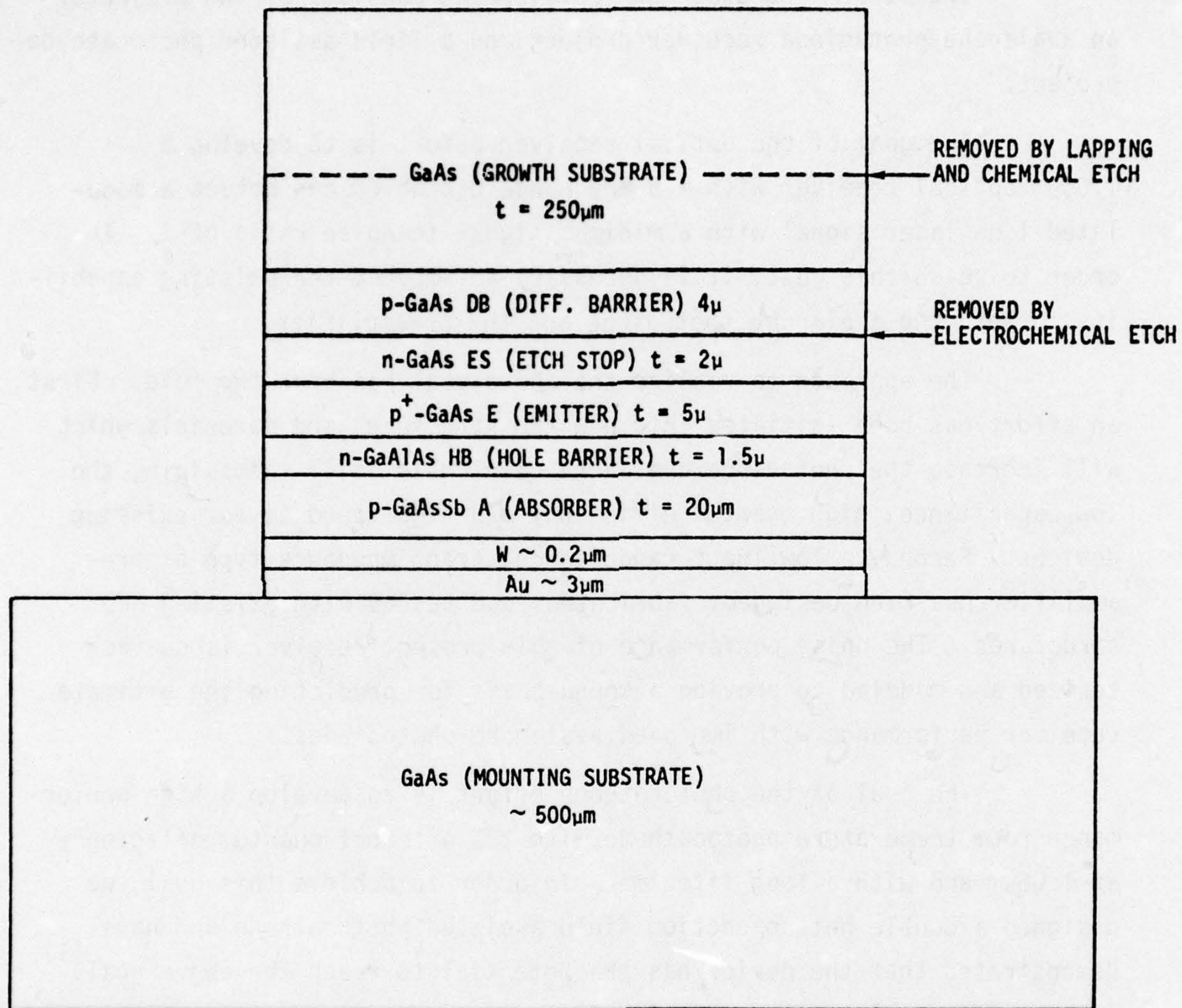

Fig. 2.1 **The proposed new device structure in which the epitaxial structure is eutectically bonded, absorber down, to a second GaAs substrate. The original GaAs growth substrate is then selectively removed by a combination of lapping and chemical and electrolytic etching to expose the emitter surface.**

required in the Cs activation. A new structure was suggested as a solution to the above problem.[2] This structure is shown in Fig. 2.1 (this structure is described in detail in Section 3.2). The specific tasks of this project are the following:

1) Grow and fabricate the heterostructure device in Fig. 2.1.
2) Develop any necessary passivation layers for the exposed heterojunction surfaces.
3) Develop an activation technique (including surface cleaning by sputtering) which yields a good negative electron affinity surface, yet maintains the device integrity.
4) Demonstrate vacuum photoemission.

3.0 RESULTS

3.1 1.06μm APD Receiver

The work on 1.06 m optical receivers has been supported at this laboratory by Air Force contracts F33615-74-C-1030 and F33615-75-C-1165 and NASA contracts NAS5-23134 and NAS5-22806. The present effort is aimed at developing a high sensitivity 5 MHz preamplifier and computer model of the important noise sources effecting the performance of the receiver and a continuing effort to improve the performance of the avalanche photodiode.

The photodiodes used in the receivers reported in this work have all been fabricated from GaAsSb. The epitaxial growth techniques and performance data on these GaAsSb devices has been reported extensively in prior reports (3-4) from the contracts cited above. Devices fabricated from this material have yielded only limited and non-uniform avalanche gain. It is now believed that we have achieved the performance limit of avalanche gain in this type of lattice mismatched structures. This is due to localized non-uniform epitaxial layer thickness caused by the lattice mismatch between the GaAsSb active layer and the GaAs substrate. Since the active region must be operated near complete depletion in order to maintain a high quantum efficiency, the thin regions of the layer are completely depleted and have a high electric field with high gain. The thicker regions remain undepleted and have a much lower electric field with no gain. Because the lattice mismatch and resulting surface structure and layer thicknesses cannot be eliminated, improving performance with these devices will be difficult.

A new material which has been studied extensively at this laboratory is GaAlSb. This material, grown on a substrate of GaSb, results in about an order of magnitude improvement in lattice match over the GaAsSb-GaAs system and is expected to give much more uniform layers for avalanche photodiodes. For this reason, the main thrust of the avalanche photodiode program has been shifted to this material. The photodiode work reported here, is therefore, concerned with a discussion of the growth, processing and preliminary results on photodiodes of GaAlSb.

3.1.1 Growth of $Al_xGa_{1-x}Sb$ for 1.06μm Avalanche Photodiodes

Because it is nearly perfectly lattice matched and covers the appropriate energy bandgap region, the ternary alloy $Al_xGa_{1-x}Sb$ is very attractive for 1.06μm avalanche photodetectors. Its chief drawback has been the lack of information on both material preparation and properties. In fact, our research effort into long wavelength photocathodes[5] represents the first systematic investigation of the LPE growth conditions and opto-electronic properties of $Al_xGa_{1-x}Sb$ alloys. Previously, only very limited experimental values concerning the endpoint compositions GaSb and AlSb were available. GaSb and AlSb are known to be direct and indirect gap semiconductors with conduction band minima at 0.68 and 1.5 eV respectively. Recent work on this alloy system provides the necessary technology to consider this system for device applications.

Epitaxial layers of $Al_xGa_{1-x}Sb$ alloy composition are conveniently grown from Ga solution at temperatures near 500°C. In our work we have experimentally established for the first time the $Al_xGa_{1-x}Sb$ liquidus and solidus lines.[5] Fig. 3.1 shows the 500°C Al distribution coefficient; this gives the solid compositions we have grown from the particular melt shown. The solid compositions were determined from microprobe analysis using ZAF corrections. We have obtained the corresponding 500°C liquidus curves by visual observation of just saturated Al-Ga-Sb melts through a semi-transparent furnace; the experimental data are shown in Fig. 3.2.

Fabrication of 1.06μm avalanche photodetectors requires growth of $Al_xGa_{1-x}Sb$ alloys with bandgaps near 1.17 eV. Photoluminescence and absorption measurements have led to greatly improved understanding of the band structures within the ternary system. The results of these important measurements, and other recent work,[6-8] are shown in Fig. 3.3. The two key differences from earlier data are: (1) relocation of the GaSb X minima to 1.8 eV (from 1.1 eV) and (2) relocation of AlSb Γ and L minima from ~ 2.1 eV to 1.66 eV. Photoluminescence measurements, made over the range $0 < x < .7$, establish the location of the Γ minimum as shown, and indicate that $Al_xGa_{1-x}Sb$ is direct gap

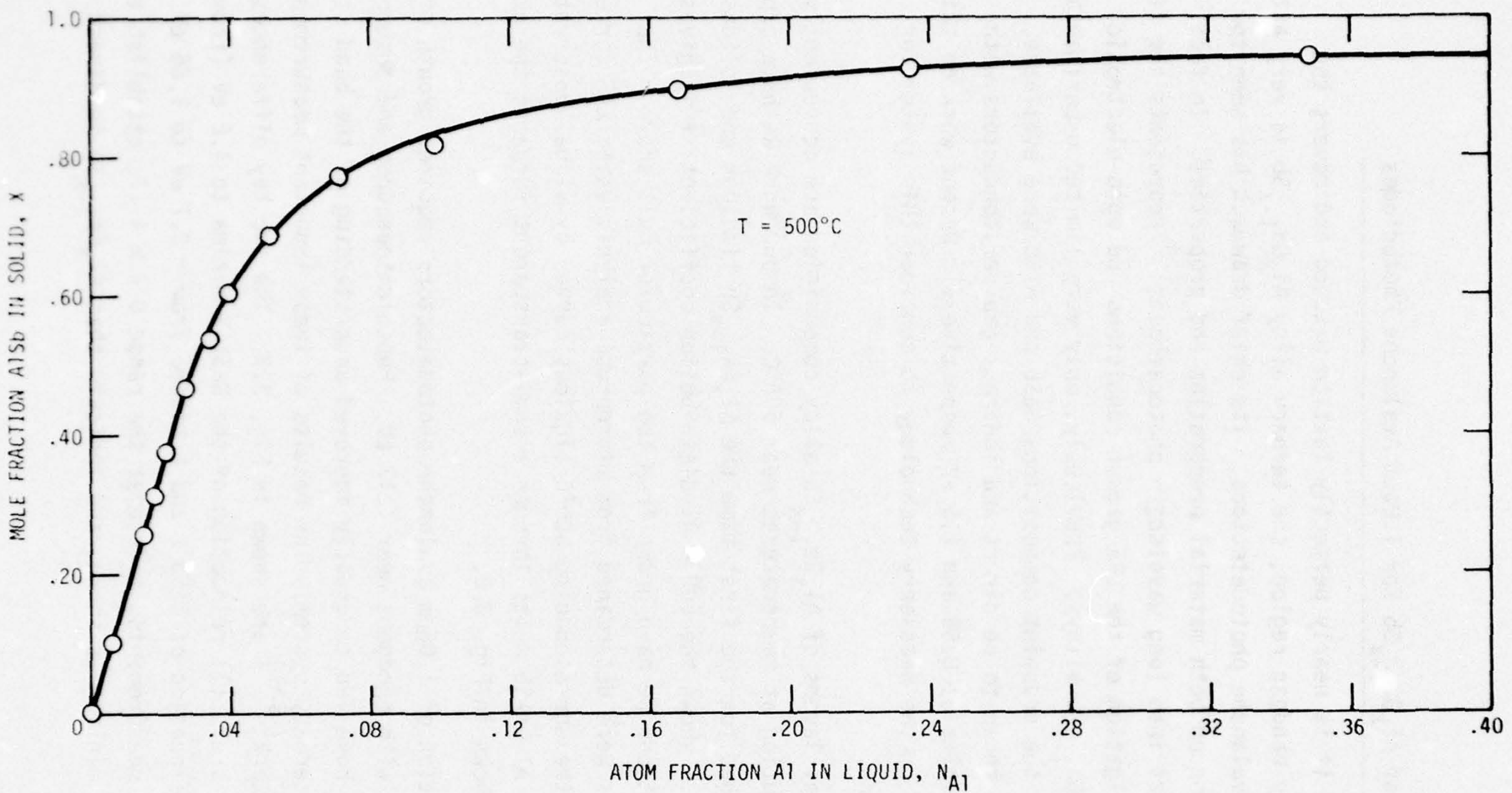

Fig. 3.1 Experimental 500°C solidus line for GaAlSb showing solid composition vs. Al composition in the liquid.

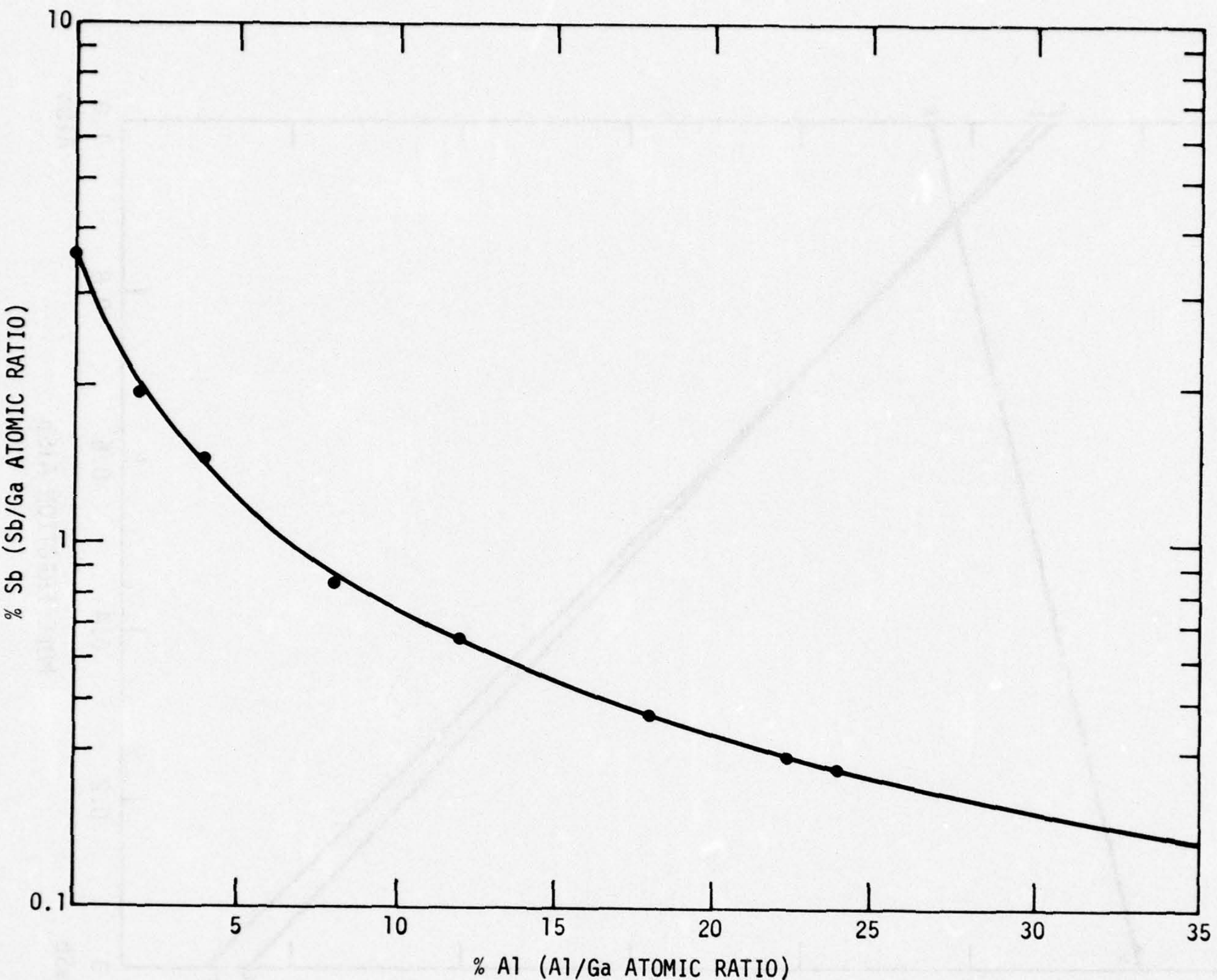

Fig. 3.2 Experimental 500°C liquidus line for GaAlSb showing melt composition vs. mole fraction of Al in the liquid.

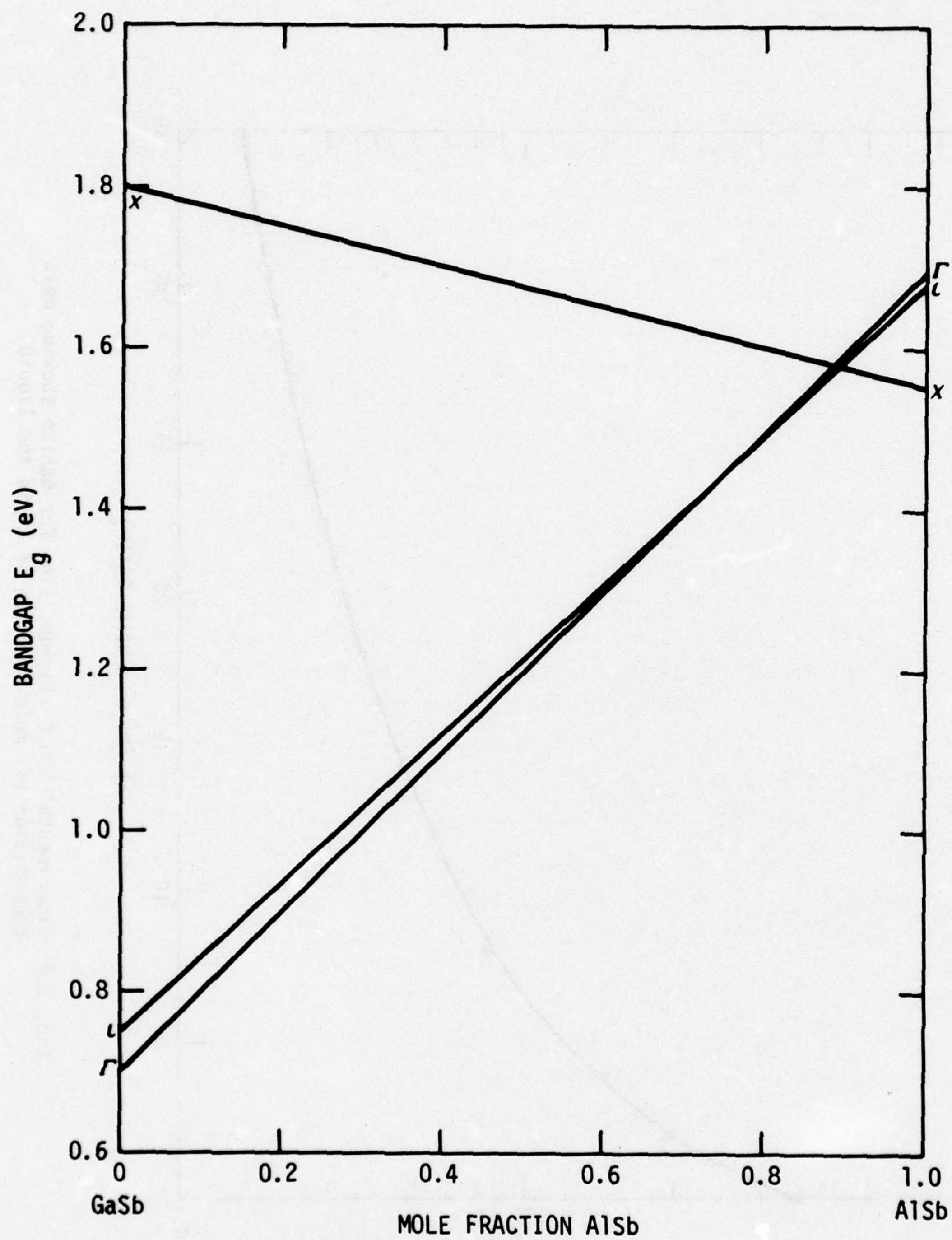

Fig. 3.3 Energy band structure vs. composition for GaAlSb.

for $x < .7$. Previous work had tentatively indicated a direct-indirect cross-over at $x \cong 0.4$ or .2 with X supposedly becoming the lowest minima in this region. If we use Eastman's recent data for GaSb ($E_X = 1.8$ eV)[9] we can generate a linear approximation for the X minima for the whole range of alloy compositions, as shown in Fig. 3.3. Clearly, X does not become the lowest minima until $x > 0.8$; this is in agreement with our photoluminescence results. To date no photoluminescence measurements have been made in the region $x > 0.7$. Using a high power argon laser (or other short wavelength laser) one should be able to experimentally locate the Γ-X cross-over and follow the X minimum out to $x = 1$, AlSb.

For 1.06μm photodetection (.17 eV) we see that alloys with $x < 0.35$ are required. Our band structure measurements discussed above now indicate that for this composition, the bandedge is direct. This is, of course, highly desirable for high speed, high quantum efficiency photodetectors. One could always obtain larger absorption coefficients by using smaller gap materials (with less Al) but this results in more dark current (increased thermal generation). The best choice is a direct gap material with bandgap just below the photon energy to be detected; $Al_{.35}Ga_{.65}Sb$ now seems to be such a material. Previous measurements on GaSb and AlSb, as we noted above, had indicated a direct-indirect cross-over at energies at, or possibly below, 1.06μm.

$Al_xGa_{1-x}Sb$ 1.06μm avalanche photodetectors have been fabricated using a "window structure" in which light is brought in to the $Al_{.35}Ga_{.65}Sb$ active layer through a contacting layer with $x > 0.35$ as shown in Fig. 3.4. The p-n mesa device can always be designed so that the surface fields in the depletion region are less than the bulk fields, thereby insuring bulk, rather than surface breakdown. Choice of an n^- or p^- active absorbing region will depend on the relative magnitudes of M_e or M_n, the electron and hole multiplication factors. These factors in turn are determined by the electron and hole ionization rates α and β: $\log (M_e/M_n) = \int_0^W (\alpha-\beta)dx$ (the high field region here extends from $X = 0$ to $X = W$). Early workers all assumed $\alpha = \beta$ for the III-V compounds, but recent measurements have shown that this is not correct.[10] Proper

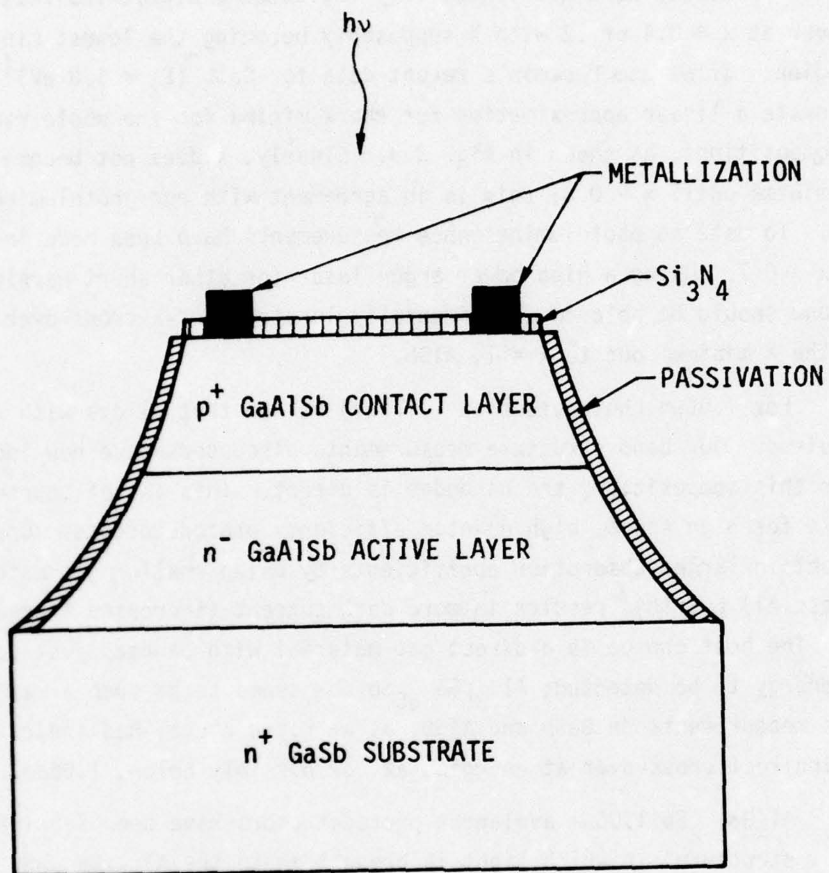

Fig. 3.4 GaAlSb lattice matched avalanche phototiode structure.

design of an $Al_xGa_{1-x}Sb$ avalanche photodetector for maximum avalanche gain and least excess noise will thus require some investigation of α and β for alloy compositions in the region of interest ($X < 0.35$).

Our work to date on AlGaSb avalanche photodetectors has centered on developing the growth and fabrication techniques and measuring the avalanche gain properties of n^- $Al_{.23}Ga_{.77}Sb$. This alloy has been the "active layer" in all of the device structures grown. Top contacting layers were either p^+ $Al_{.35}Ga_{.65}Sb$ window layers or p^+ $Al_{.23}Ga_{.77}Sb$ homojunction lattice matching layers.

The device structures were all grown at 500°C on suitably prepared n^+ GaSb substrates. Several test growths of single n and p $Ga_{.77}Al_{.23}Sb$ layers established the doping levels required. C-V measurements on Te doped n^- layers showed that $8\times10^{15} < n < 1\times10^{16}$ cm^{-3} could be achieved with a Te mole fraction in the melt, $X_{Te}^{\ell} = 2\times10^{-9}$. This low concentration was obtained by using 1×10^{18} cm^{-3} Te doped GaSb substrate material as the Te source. Infrared reflectivity measurements on Ge doped p^+ layers established that $p = 2\times10^{18}$ cm^{-3} could be reproducibly achieved with a Ge mole fraction in the melt, $X_{Ge}^{\ell} = 1\times10^{-4}$. The layers were grown from melts saturated for 2-3 hours at ~ 500°C [500°C growth temperature]. After re-equilibration at 500°C, growth was initiated by slow cooling at rates 1.5°C/min<dT/dt<4°C/min. Typical growth rates of 2-3μ/min were achieved. The two layers are grown sequentially in a multicompartment boat by standard LPE techniques.

After removal from the furnace, the layer thicknesses are measured by cleaving a cross-section of the layer, staining in the A-B etch[11] and then taking a photomicrograph of this cross-section. Since the GaSb substrate is opaque out to 1.8μm, IR microscopy or transmission measurements cannot be used to examine the structure in the same manner as the GaAsSb devices were examined. After layer thickness is determined, the compositions are measured by x-ray emission in the SEM (i.e. microprobe) and then passed on for device fabrication.

3.1.2 AlGaSb Avalanche Photodiode Fabrication

In this section the processing sequence for fabrication of the GaAlSb devices is described. Each step in the fabrication must proceed very carefully to avoid unnecessary problems that might occur. A clean sample surface is essential before metals are evaporated. Au-Ge and Ag-Mn alloys are used on n-type and p-type GaSb or GaAlSb layers respectively for metallization. The metallization on GaAlSb layers is an E-beam evaporated ring pattern so that the light may enter from the top layer side as shown in Fig. 3.4. The metal contacts are alloyed and the ohmic contact resistance is checked. Au is electroplated over the metal contacts to protect them from pressure contacts or thermocompression bond contacts. The mesa is then chemically etched and the surface is passivated to protect the exposed p-n junction and to decrease the surface leakage current. To obtain maximum quantum efficiency, Si_3N_4 is deposited over the light entrance window on the GaAlSb layer side for the antireflection coating. Careful monitoring of the etch depth is important to obtain the desired mesa geometry which reduces electric field concentration at the p-n junction. The depth of the mesa is measured under a microscope after each mesa etch and compared to the layer thickness which is known from the measurement of the cleaved and stained edge of the layer. After the mesa etch and passivation, the device is epoxy bonded into our standard photodiode package and electrical and optical characterization are carried out.

3.1.3 GaAlSb Avalanche Photodiode Measurements

To determine the device performance characteristics various types of experimental measurements are taken. These range from simple volt-ampere (I-V) curve measurements to sophisticated scanning electron microscope studies. These measurements provide the essential feedback for the material growth and device fabrication portion of the work. Volt-ampere (I-V) measurement provides directly the leakage current of the device (which is the low light level performance limiting parameter), and shows up problems due to surface leakage, contacts, irregular breakdown, anomalous surface photo effects, etc. The I-V measurement is carried out using a TEKTRONIX 576 semiconductor curve tracer

with a specially designed probe station. For accurate permanent records of I-V characteristics, a picommeter and x-y recorder is used. The advantage in using the 576 is in versatility, speed, and convenience of use as compared with the x-y recorder method. C-V measurements provide both the capacitance value as a function of bias voltage (low capacitance is essential for microwave performance), and the doping profile. Using the MDC automatic doping profiler, C-V and carrier concentration vs. depletion width are plotted on x-y recorder. The result is fed back to the material growth to obtain the values necessary for an optimum photodiode.

The narrow band photoresponse characteristic of the GaAlSb photodiode is critically dependent on alloy composition of both of the GaAlSb layers. In order to provide the data feedback necessary to attain the goal of high quantum efficiency at 1.064μ, spectral photoresponse measurements are made on virtually every device with acceptable I-V characteristics. A modified Cary 14R spectrophotometer is used to make this measurement. The diode is placed in a special probe station and mounted inside the spectrophotometer for light to fall on the diode. The signal from the device is fed into the current amplifier to make relative quantum efficiency vs. wavelength measurements on a diode.

The key APD optical measurements of quantum efficiency, quantum efficiency uniformity (spatial response), pulse response, avalanche gain and gain uniformity, as well as overall receiver performance are made using a Nd-YAG 1.064μ laser source and a scanning light microscope (SLM) system. This system has been described in our earlier report.[3] SLM system scans a finely-focused laser beam over the photodiode in a TV-like raster pattern and displays the spatial variations of the desired physical parameter on an oscilloscope display which is either intensity or deflection modulated by the signal. The display appears very much like a scanning electron microscope.

The preliminary results from one of the GaAlSb diodes is described. This is one of the first diodes fabricated from this alloy, however, the results look encouraging from the standpoint of eliminating the surface features and layer non-uniformities which have limited the avalanche gain of

the earlier GaAsSb devices. A photoresponse curve for a GaAlSb photodiode (structure in Fig. 3.4) is shown in Fig. 3.5. The short wavelength cutoff is determined by the absorption of light in the top GaAlSb layer which creates photoelectrons that are not collected by the p-n junction. This cut-off is $\sim 0.92\mu m$. The long wavelength cut-off is determined by the transmission of light completely through the active GaAlSb layer such that no photoelectrons are generated. This cut-off is $\sim 1.2\mu$. The almost flat response near $1.06\mu m$ assures a maximum $1.06\mu m$ quantum efficiency for the device.

Avalanche gain measurements have been taken on both GaSb (substrate)-GaAlSb p-n junction diodes and GaAlSb-GaAlSb p-n junction diodes. The GaSb-GaAlSb diode showed uniform gain of ~ 2.5 before the response became noisy. GaAlSb-GaAlSb diodes had low breakdown voltage which prevented any significant measurement of gain. From the doping profile measurement a carrier concentration of $3x10^{16}$ cm^{-3} was obtained as shown in Fig. 3.6. The estimated breakdown voltage for this carrier concentration is 40-50 V with $\sim 3\mu m$ depletion width. From the current-voltage measurement, the breakdown voltage is only 12 V. This problem has been analyzed using the SEM and the SLM.

In the Scanning Electron Microscope (SEM) induced current mode, the exposed p-n junction is examined. A finely-focused electron beam is scanned across the surface of the junction. At the point where the beam strikes, a large number of hole-electron pairs is generated. If these hole-electron pairs are generated in the depletion region or within a diffusion length of either side of it, the carriers will transit across the junction giving rise to a measurable junction current. This data is presented either in the form of a video display or simply as an oscilloscope trace of the induced current as a function of position. Figure 3.7 a) and b) show the SEM induced current mode micrograph. The junction is very uniform as seen in the brightness and in the width of the junction. There are no obvious defects or inclusions seen in the junction or on the surface to cause the low break-down voltage.

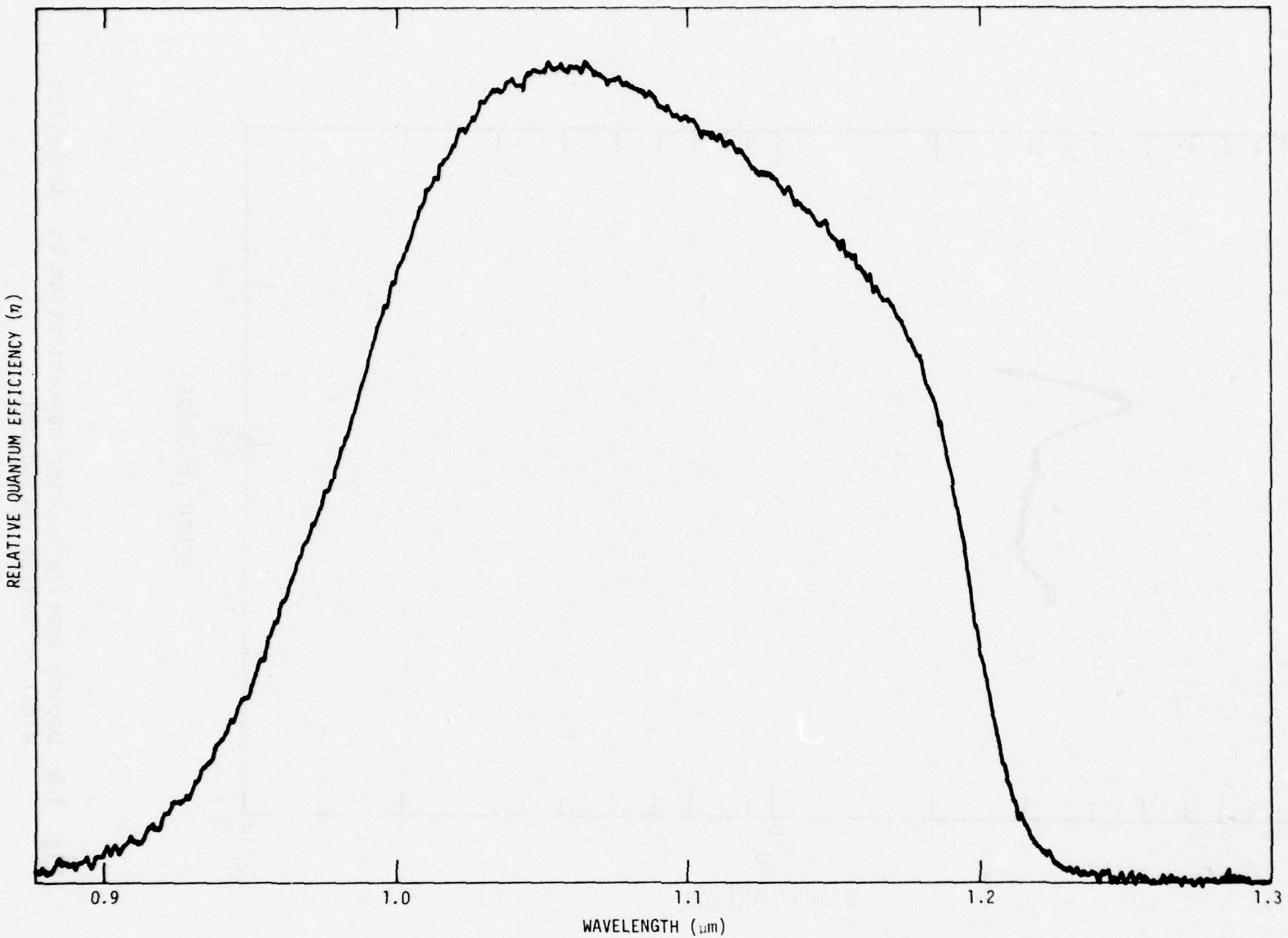

Fig. 3.5 Relative quantum efficiency vs. wavelength of GaAlSb photodiode.

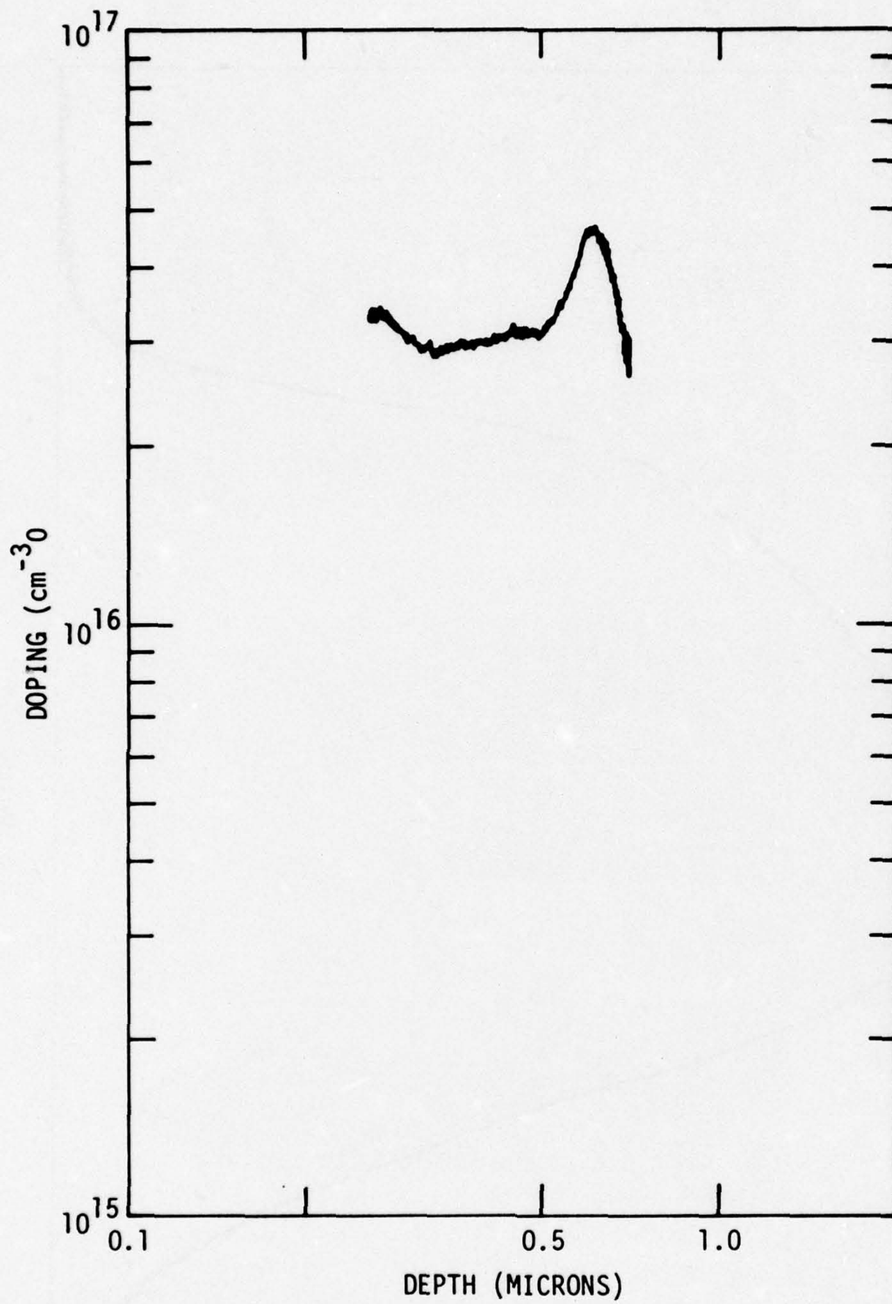

Fig. 3.6 Doping profile carrier concentration vs. depletion width of GaAlSb photodiode.

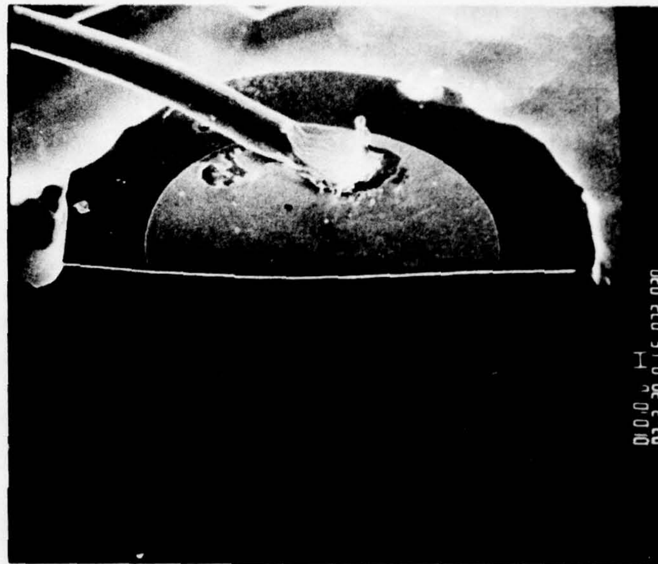

(a)

(b)

Fig. 3.7 Scanning Electron Microscope induced current mode photomicrograph of GaAlSb photodiode.

The Scanning Light Microscope (SLM) is similar to the SEM except that a finely focused 1.06μ Nd-YAG laser is scanned across the diode. Instead of looking at the exposed cross-sectional area of the diode, the SLM scans the whole p-n junction depletion area. An intensity modulated SLM micrograph of the diode is shown in Fig. 3.8. Intensity or brightness corresponds to the amplitude of photocurrent and X and Y axis corresponds to the X and Y dimension of the diode (1 mil per div.). This reveals a fairly uniform response (the dark area on the left is the probe). This photograph shows a well defined mesa with no bright ring around the outer edge. Such a bright ring occurs if either a surface inversion layer forms or surface breakdown occurs. Neither of these appears to happen, thus no obvious surface problem is limiting the avalanche multiplication. In examining the bulk area of the diode, no obvious "hot spots" (microplasma type defect) appears which would create current leakage and limit the gain. At this point, there is no obvious gain limitation and further diodes will have to be examined.

3.1.4 5 MHz APD Receiver Model

At this point in the receiver development program, three 5 MHz prototype receivers have been fabricated, and detailed noise measurements carried out on two of these. The detailed circuit description along with the development of the apparatus for fabrication of the critical components (APD, circuit substrate, feedback resistor element) were described in the final report[4] for contract no. F33615-75-C-1165. Only a summary description of the receiver is made here for reference to the noise modeling work on these receivers.

As illustrated in Fig. 3.9, the preamplifier for the receiver is a transimpedance type amplifier. Major requirements for the preamplifier are the following:

1) The open-loop frequency response of the amplifier ($A_1 x A_0$) must be much greater than the required overall closed-loop bandwidth of 5 MHz. This is in order to prevent undesirable poles in

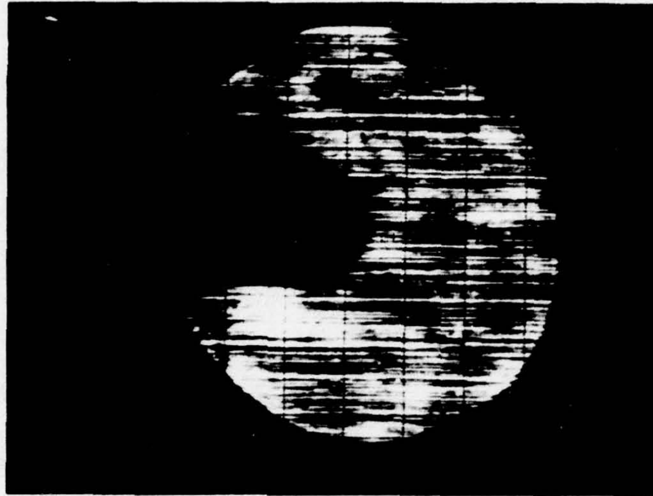

Fig. 3.8 Scanning Light Microscope intensity modulated photomicrograph of GaAlSb photodiode response to 1.06μm laser.

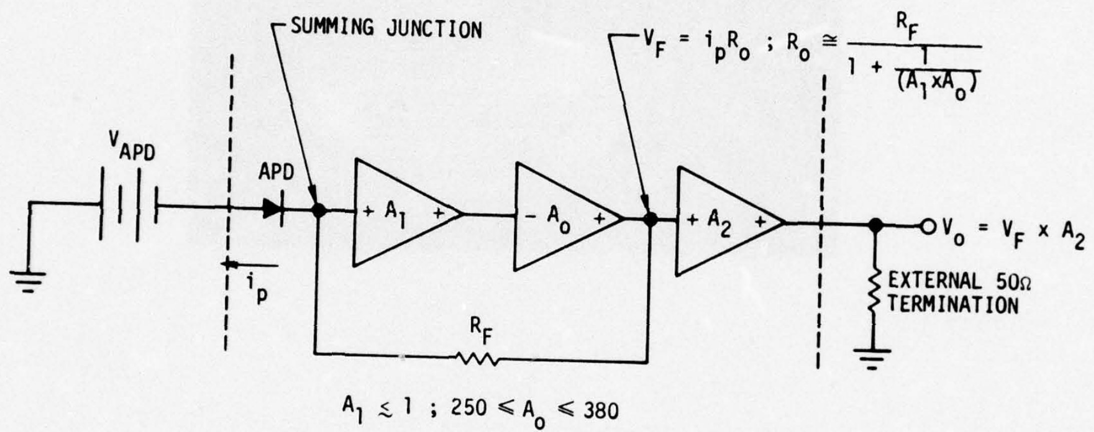

Fig. 3.9 5 MHz receiver block diagram arrangement of component parts of receiver.

the feedback loop which lead to oscillation. The open-loop frequency response is dominated by A_o.

2) With low photodiode avalanche gain, the dominating noise sources are the thermal current noise of the feedback resistor, R_F, and the current noise induced by the voltage noise of the 1st stage amplifier A_1, (e.g. $i_{nj} = \sqrt{\frac{4kT}{R_F}}$ Amps/$\sqrt{Hz}$, $i_{ne} \propto \omega C_i$ Amps/$\sqrt{Hz}$; $\omega = 2\pi f$). Also, since the combination $R_F C_i$ forms a low pass filter, R_F and C_i are related by $R_f = \frac{A_1 A_o}{2\pi \Delta F C_i}$. From the above equations we see that in order to minimize i_n, we must maximize R_F. It is clear from this and also from the relationship of i_{ne} to C_i, that the value of C_i is of central importance and must be made as small as possible. C_i is composed of the photodiode capacitance (C_{APD}), the input capacitance of the preamplifier, A_1, and stray capacitance from the summing point to ground. The APD capacitance is determined by device geometry and bias voltage and is already minimized. The input amplifier capacitance determines the type of active element that must be used. The stray capacitance is held to a minimum by the circuit layout. All these contributions combine to give an equivalent input capacitance of less than 1 pF in our design.

3) The ultimate closed-loop frequency response is limited by the stray capacitance shunting R_F (e.g. $\frac{1}{2\pi R_F C_F}$). Using the optimum value for R_F, as described above, we find that we are limited to $C_F \cong 1 \times 10^{-15}$F in order to achieve the desired bandwidth. This value of stray shunting capacitance is orders of magnitude less than appears across commercially available resistors of any kind known. Thus, fabrication of this feedback element is a major factor in developing a high sensitivity receiver.

The amplifier A_2 is a current amplifier designed to isolate the output of A_o from capacitance loading and enable the receiver to drive 50Ω lines. In the first and second prototypes, this section had unity voltage gain. In the

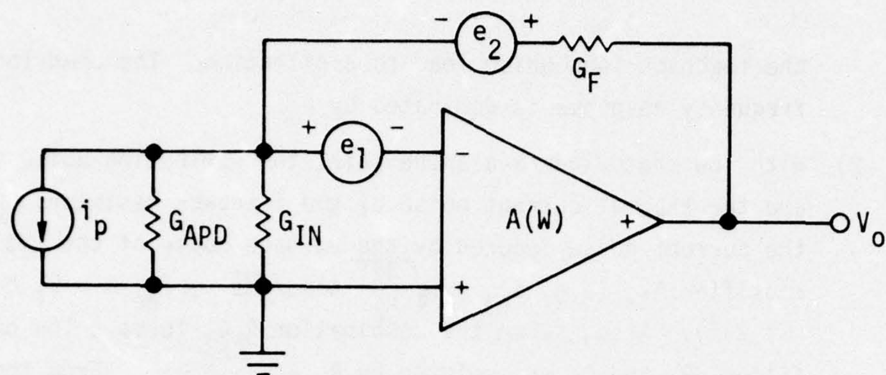

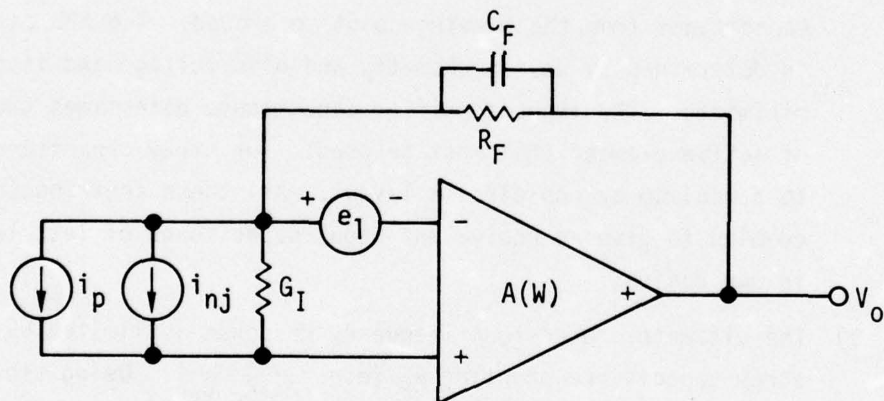

Fig. 3.10 Model used for analysis of signal and noise response. e_1 is the equivalent input noise voltage generator of the preamp, e_2 is the Johnson noise voltage generator of the conductance G_F. In (b), G_I replaces the input conductance of the preamp and the conductance of the APD and i_{nj} replaces e_2.

third prototype, the voltage gain was made 0.1 in order to increase the dynamic range of the receiver. This, of course, does not degrade the signal-to-noise ratio since the noise at the output of A_o is considerably greater than the equivalent input noise of this section.

The voltage gain section, A_o, must have extremely high gain-bandwidth product so as not to introduce additional phase shift in the 5 MHz passband. Only then is the advantage of the high effective load resistance and resulting lower noise performance of the transimpedance amplifier realized. The best of the three prototypes so far constructed has a gain-bandwidth product of about 3.6 GHz.

The input amplifier A_1 must exhibit low equivalent input voltage noise spectral density, e_n, and very low capacitance, C_i. Since the amplifier noise (mostly from this stage) is proportional to e_n and C_i, we believe that to first order, the contribution from these elements is somewhat interchangeable. Thus, in the first prototype we used a T.I. 3N204 Mosfet $e_n \simeq 5\times10^{-9}$ $V/\sqrt{Hz}$, $C_{gs} \simeq 5$ pF, and in the second and third, a Signetics SD-200 with $e_n \simeq 20\times10^{-9}$ $V/\sqrt{Hz}$, $C_{gs} \simeq 2$ pF. These values are nominal manufacturers specifications and have not been measured directly by us.

The resistance element R_F is a thin film "cermet" resistor and was fabricated by us using a high-vacuum evaporation system designed specifically for this purpose. Measurements on the receiver imply the feed thru capacitance, C_F, is between 1 and 2×10^{-15}F for these resistors.

A reasonable model for the receiver for both signal and noise is represented in Fig. 3.10 a) and b). Fig. 3.10 a) is the generalized model with e_1 and e_2 being frequency dependent voltage noise sources of the amplifier and of the feedback element G_F respectively. The amplifier $A(\omega)$ is considered to have infinite input impedance, zero output impedance and zero noise. Its frequency dependence is taken to be: $A(\omega) = \frac{A_o}{1 + j\frac{\omega}{\omega_A}}$; where A_o is the low

frequency gain, and ω_A is the amplifier 3dB frequency. This model is drawn more explicitly in Fig. 3.10 b) where G_F is modeled with R_F in parallel with C_F, and e_2, the Johnson noise voltage term is converted to its equivalent frequency independent current form and indicated in parallel with I_p at the input of the amplifier.

G_{IN} for the devices used in the input stage is virtually purely capacitive, as is G_{APD}, so that their combination, G_I, in Fig. 3.10 b) is considered as a capacitance in the analysis. The forward transimpedance for this model is given by:

$$V_o = \frac{(i_p + i_{nj})\left(\frac{1}{G_F}\right)}{1 + \frac{1}{A}\left(1 + \frac{G_I}{G_F}\right)} + \frac{e_o\,(G_F + G_I)}{G_F + \frac{1}{A}(G_F + G_I)}$$

where $i_{nj} = \sqrt{\frac{4kT}{R_F}}$ Amps/$\sqrt{Hz}$,

$$G_I = j\omega C_I, \quad G_F = \frac{1}{R_F} + j\omega C_F$$

$$A = \frac{A_o}{1 + \left(\frac{\omega}{\omega_A}\right)^2}$$

Note that in the ideal case of zero noise, zero input conductance, and zero C_F,

$$V_o \simeq \frac{i_p R_F}{1 + \frac{1}{A}} \equiv i_p R_o$$

A computer program was written to gain further insight into the behavior of the signal and noise responses vs. frequency for various choices of the above parameters. Independent measurement of the above parameters is done for the receivers actually constructed and the noise model adjusted to fit this data.

In this way, the measured noise spectra are compared to calculated ones to test the model and then be able to use this model to improve future receivers by optimizing the receiver design.

The computer program for the noise model was written in "TEK-BASIC". This language is an adaptation of the "BASIC" language and was developed by the Tektronix Company to be used in conjunction with their Digital Processing Oscilloscope System. This language has strong graphics capability which is quite useful when the results of several calculations are to be compared. The input parameters for the program are: R_F, C_F, A_o, F_o.

The transimpedance equation is solved in two parts. First, it is assumed that $i_{nj} = e_i = 0$ and the equation is considered as $(\frac{V_o}{i_p}) = a + jb$. The real (a) and imaginary (b) parts of this equation are computed in 512 equal frequency increments of 20 KHz each and stored separately in arrays in the computer memory. The frequency runs from -51.2 MHz to +51.2 MHz, however, only the positive frequency span is displayed. An example of this is shown in Fig. 3.11 a). The reason negative frequencies are included is to make subsequent calculations, involving transformations from the frequency domain to the time domain and vice versa, self-consistant. The arrays containing the real and imaginary parts of $(\frac{V_o}{i_p})$ are squared, summed and the square root of the result taken to yield $|\frac{V_o}{i_p}|$. The inverse fourier transform of this array is then taken, (a function in the Tek-basic Software) and the result normalized to yield the impulse response of the circuit. The amplifier frequency dependent noise is next computed by letting i_p and i_{nj} be zero in Eq. (3) and squaring the result. This result is the multiplier to be used in the computation of the noise spectra in the second half of the program.

In the second half of the program, an additional parameter, e_n, is entered. This is the expected noise voltage spectral density of the input stage of the amplifier in volts/$\sqrt{Hz}$. The real and imaginary parts of the transimpedance are individually squared, then added. The square root of the result yields the closed-loop signal frequency response. The 3dB frequency of this array is computed and outputed for comparison with measurement. Also at

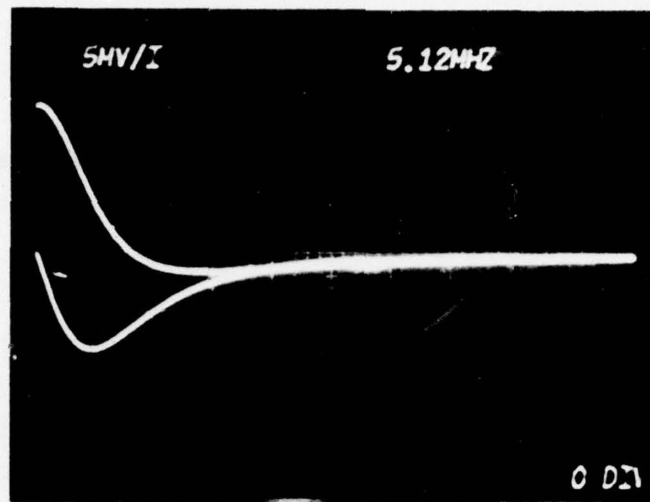

(a)

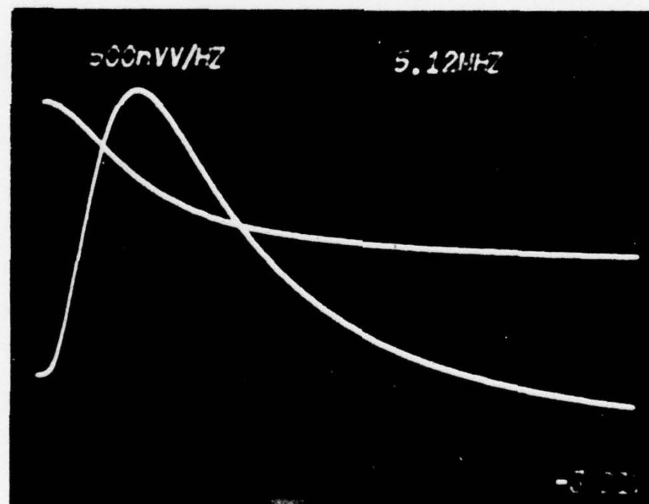

(b)

Fig. 3.11 Outputs of noise analysis computer program

(a) real and imaginary parts of transimpedance

(b) sum of squares of real and imaginary parts of transimpedance; (magnitude)^2 of frequency response and output noise voltage vs. frequency.

this point, the Johnson noise spectral density of R_F in Amps/$\sqrt{Hz}$ is computed and outputed.

The important calculation in this section is the output noise spectrum. This is accomplished simply by multiplying the square of the Johnson noise spectral density with the square of the magnitude of the transimpedance, and adding this to the square of the voltage noise spectral density multiplied with the voltage noise multiplier computed in the first half:

$$(V_{on}(f))^2 = i_{nj}^2 \times \left|\frac{V_o}{i_p}\right|^2 + e_n^2 \times (B(f))^2$$

where B is the voltage noise multiplier.

This result is outputed in an array (Fig. 3.11 b)) and can be compared with the measured spectral dependence of the output noise. Also, the square root of the integral of this array yields the total output noise which can be compared with the observed total output noise. As an added feature, since the normalized impulse response and the charge sensitivity $(\frac{V}{Q})_p$ are known, the minimum number of electrons detectable in a pulse is computed from $N_o = \frac{V_o}{q\ (V/Q)_p}$. This, of course, divided by η, (the quantum efficiency) yields the minimum number of photons in a δ-function pulse of light which can be detected by the receiver.

3.1.5 5 MHz APD Receiver Measurements

The principle measurement instruments employed were a Tektronic Digital Processing Oscilloscope (DPO) system, and a Tektronix Model 7L13 Spectrum Analyzer (~ 1 KHz to 1.8 GHz). In addition, a HP Model 313A tracking oscillator and 312B selective voltmeter combination was used as well as a HP Model 3400-A RMS voltmeter.

The first important parameter to be measured on the receiver is the *open-loop gain-phase vs. frequency*. The receiver configuration for this measurement is indicated in Fig. 3.12. Here, the feedback loop is broken and a signal

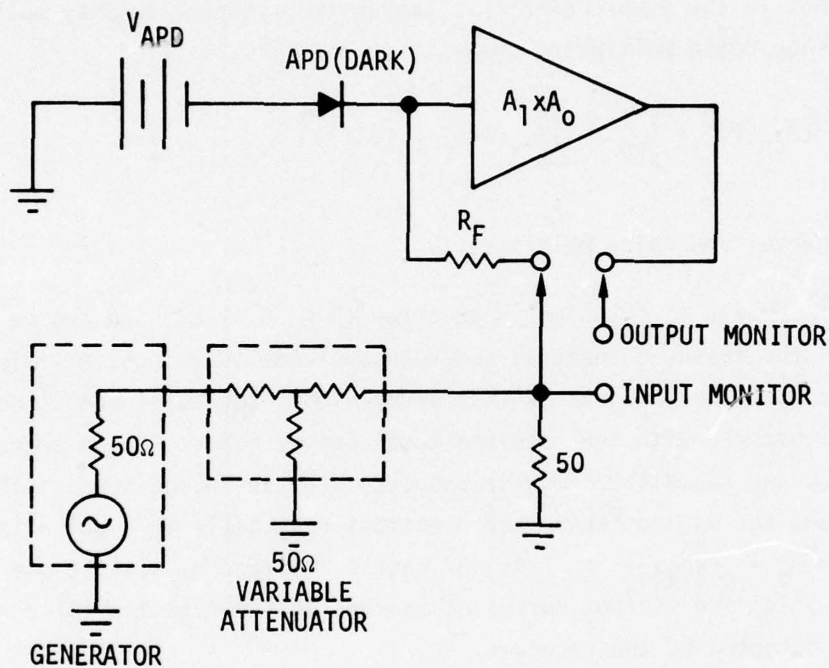

Fig. 3.12. Experimental configuration for measurement of open loop gain-phase.

is injected into the feedback resistor as shown. The magnitude and phase of the output signal is then compared with this input to determine the amplifier and phase-shift. This measurement is relatively easy in the passband of the amplifier where the output signal is large, and can be accomplished with a Vector voltmeter. In fact, the -3dB point determined by $f_{-3dB} = \frac{A}{2\pi R_F C_i}$ (where C_i is the total equivalent input capacitance of the receiver, including C_{APD}) can be measured this way and C_i thus determined. However, important information regarding the phase-margin and hence stability is contained in the response at frequencies much higher than the f_{-3dB} point. At these higher frequencies, the output is small in magnitude and almost totally buried in noise. Thus direct measurement of gain and phase is impractical. One of the functions contained in the DPO software is a correlate function. The cross-correlation of an equal number of cycles of two sine-wave functions of equal frequency is illustrated in Fig. 3.13. From the magnitude and location of the peak of this function, both the ratio and phase of these sine-waves can be determined. Since the computation for each point of the cross-correlation utilizes the whole input waveform, a considerable increase in signal-to-noise ratio is achieved. This point is illustrated in Fig. 3.13. Fig. 3.13 a) shows the two sine-waves used in obtaining the cross-correlation function (Fig. 3.13 b)). Note that even though one sine-wave is unrecognizable in Fig. 3.13 a), the cross-correlation function in Fig. 3.13 b) is very clear. By utilizing the correlate function in the DPO, measurements of open-loop gain-phase were performed at frequencies in excess of 10 MHz and the behavior of the phase near the point at which the gain approaches zero were observed.

The closed-loop frequency response of the receiver could be measured directly if a 10 MHz sine-wave modulated 1.06μm light source were available. Since such a light source is not available at our laboratory, we had to devise another technique for this measurement.

A special top cover for each receiver box was fabricated in which a shielded cable was supported with its central conductor about 0.1" from the input point of the amplifier (see Fig. 3.14 a)). Thus a small capacitance (C_c) was formed. The value of this capacitor was determined by injecting a triangular waveform and observing the output square wave. The value of C_c is

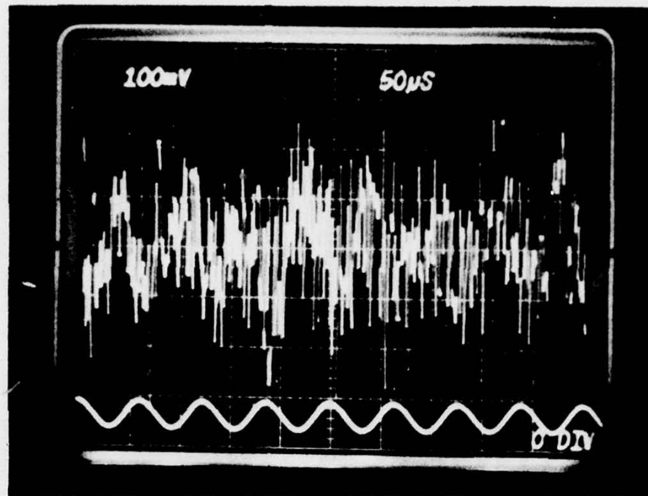

(a)

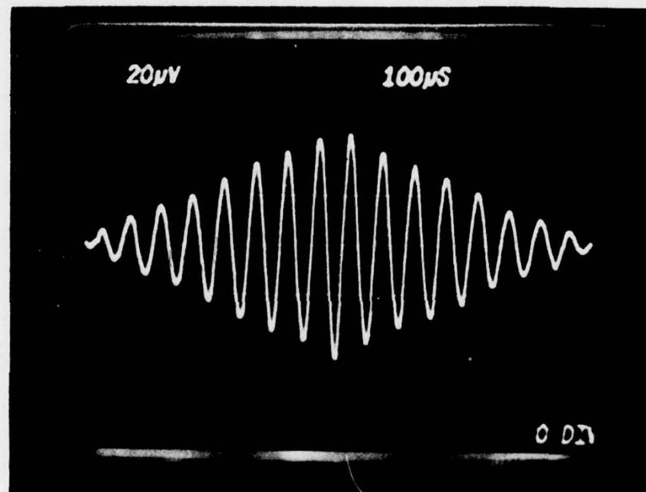

(b)

Fig. 3.13(a) 8 cycles of two sine waves of equal frequency. One sine wave totally buried in noise.

(b) Cross-correlation of the two sine waves in (a).

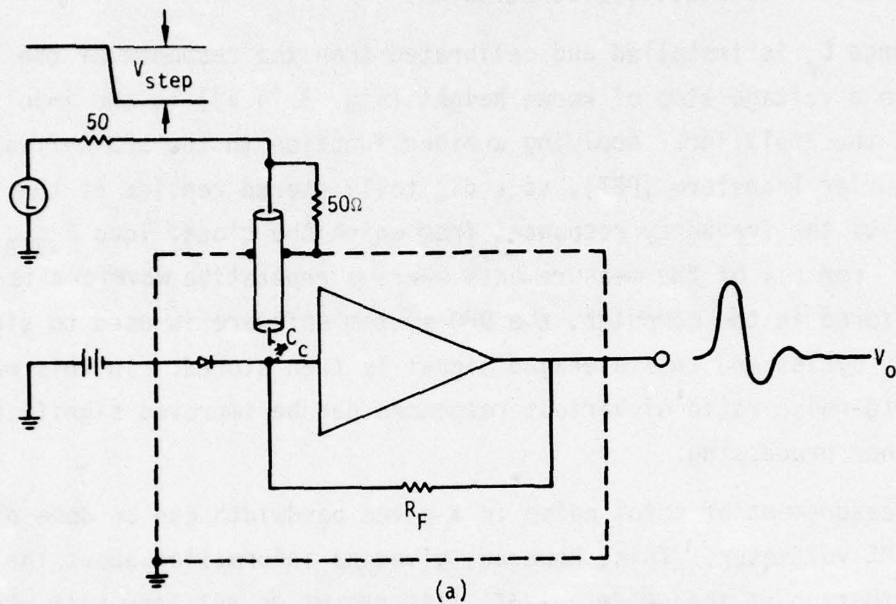

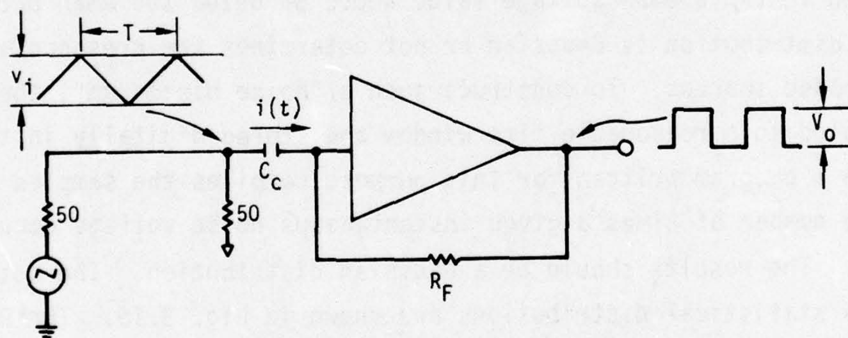

$$v_i = \frac{dv_i}{dt} \times t = \frac{dv_i}{dt}\,(T/2) \Longrightarrow \frac{dv_i}{dt} = \frac{2v_i}{T}$$

$$v_o = R_o\, i(t) \;;\; i(t) = C_c \frac{dv_i}{dt} \Longrightarrow v_o = R_o C_c \frac{dv_i}{dt}$$

$$\boxed{C_c = \frac{v_o}{R_o \left(\frac{dv_i}{dt}\right)}}$$

(b)

Fig. 3.14. (a) Test capacitor for measuring impulse response and (b) its calibration.

then obtained as indicated in Fig. 3.14 b). This value was of the order of 10^{-15} F for all three receivers constructed.

Once C_c is installed and calibrated then the response of the amplifier to a voltage step of known height (Fig. 3.14 a)) is the impulse response of the amplifier. Applying another function in the DPO software, the Fast Fourier Transform (FFT), to a digitally stored replica of this impulse response gives the frequency response, from which the closed loop F_{-3dB} can be determined. For all of the measurements where a repetative waveform is to be digitally stored in the computer, the DPO system software is used to signal average many cycles and this averaged signal is then stored. In this way, the signal-to-noise ratio of various responses can be improved significantly before further processing.

Measurement of total noise in a given bandwidth can be done directly by a true RMS voltmeter. This, however, gives no information about the statistical distribution of the noise. That is to say we do not know with what frequency a given instantaneous voltage value above or below the mean occurs. Whether this distribution is Gaussian or not determines the presence or absence of spurious noise sources. To construct such a "Noise Histogram", the output noise is sampled in a reasonable time window and stored digitally in the DPO memory. Then a program written for this purpose compiles the sampled noise and plots the number of times a given instantaneous noise voltage occurs vs. that voltage. The results should be a Gaussian distribution. The actual noise and its statistical distributions are shown in Fig. 3.15. The RMS voltage of the noise is equal to the standard deviation of the distribution as shown in Fig. 3.15 a). The measured distribution is the lower curve in Fig. 3.15 b). The log of the measured distribution is taken and compared to a curve of the log of a true Gaussian with the same standard deviation as measured on the HP voltmeter. The agreement between the measured histogram and predicted Gaussian distribution is excellent.

The most important noise measurement is the output noise spectrum, since this allows us to make a detailed comparison with the spectrum predicted by the receiver model. The most convenient way to make this measurement has

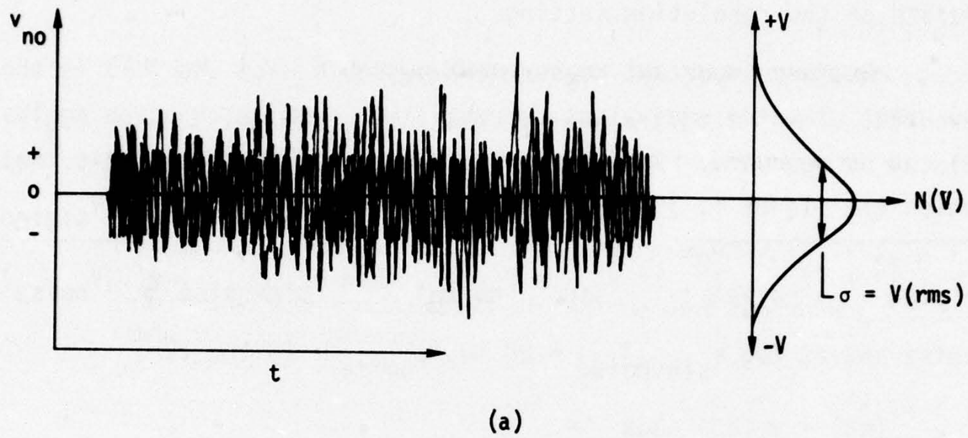

(a)

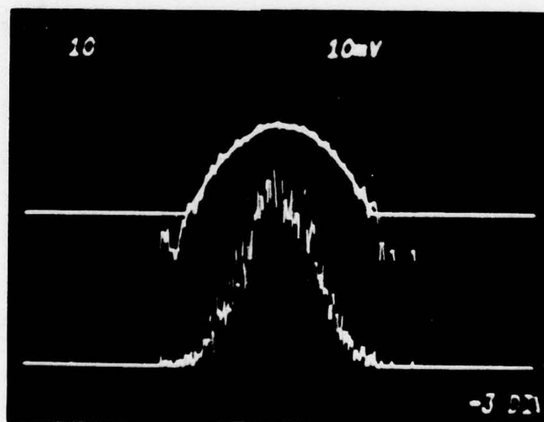

Fig. 3.15. (a) Noise output and its statistical distribution.

(b) Measured statistical distribution of output noise, its log superimposed with log of a Gaussian distribution.

been to use a Tektronix 7L13 spectrum analyzer. This instrument has a calibrated vertical scale in both log and linear modes. In addition, the noise-bandwidth of the several resolution-bandwidth settings of the instrument have been calibrated. Thus the noise spectral density at any frequency is simply the actual measured noise amplitude divided by the square root of the noise-bandwidth of the resolution setting.

Another important measurement possible with the 7L13 is the direct measurement of noise equivalent current (NEI) from which noise equivalent power (NEP) can be computed. By definition, noise equivalent power is that power at which the signal is just equal to the noise. In general: $V_{sig+noise} = \sqrt{(V_{sig})^2 + (V_{noise})^2}$, if $V_{sig} = V_{noise}$, then $V_{sig+noise} = \sqrt{2(V_{noise})^2} = \sqrt{2}$ noise and $20 \log V_{sig+noise} = 20 \log V_{noise} + 20 \log \sqrt{2}$

$$V_{s+n}(dB) = V_n(dB) +3dB$$

To make this measurement, the spectrum analyzer is centered at some convenient frequency and a suitable resolution bandwidth is selected; a sinewave at this same frequency (f_o) is injected into the preamp through C_{c_1} resulting in an input current of $i = C_c \frac{dv}{dt} = C_c \frac{d}{dt} (V_o \operatorname{Sin} \omega_o t) = C_c V_o \omega_o \cos \omega_o t$. Now as the output of the amplifiers is monitored on the spectrum analyzer, the sine-wave amplitude is reduced until the display of f_o is 3dB above the noise at f_o. The RMS amplitude of the sine-wave current into the preamp is now equal to the noise current:

$$NEI = \frac{C_c V_{3dB}(rms)\omega_o}{\sqrt{\Delta F}}$$

, where ΔF is the spectrum analyzer noise bandwidth.

Of course $NEP = \frac{h\nu}{\eta}(NEI)$. If this is repeated at different frequencies, a plot of NEI or NEP vs. frequency can be made.

Table 1 shows some of the actual measured parameters of the three prototypes that were fabricated. Fig. 3.16 a) shows the actual frequency response for receiver #3 determined by operating on the impulse response with the Fast Fourier Transform (FFT) on the DPO. Fig. 3.16 b) shows this corrected to a dB scale and plotted against the log frequency. The value at low frequency corresponds to $\frac{V_o}{i_p} = R_o \simeq 12.4x10^6$. The peaking observed in the passband is a typical second order (2-pole) response transfer function. This peaking is caused by reduced phase-margin. In an ideal second order function, 3dB of peaking is the result of a damping ratio of about 0.4 which corresponds to a phase-margin of 45°.

To observe the effect of stray shunting capacitance of the feedback resistor on the response, a new circuit model was made (Fig. 3.17 inset) in which noise was neglected, but G_F, the feedback conductance was replaced by a two-part network including C_{sh} . Also in this model the input (A_1) amplifier was modeled explicitly. To write the transimpedance of this model would be exceedingly tedious since four nodes are involved. This task is simplified by the powerful software in our APL time-shared computer. The Admittance Matrix (A-Matrix) of the circuit without feedback was written and the A-Matrix of the feedback network was also written. These matricies were entered into a circuit analysis program on this computer which is capable of combining the matricies to yield the A-Matrix of the feedback circuit. The transimpedance of this circuit is then simply the A_{21} term of this A-Matrix. The magnitude of this term plotted against frequency for a suitable set of parameters ($C_F = 1x10^{-15}F, C_{SH} = 1x10^{-15}F$) is shown in Figs. 3.17 and 3.18. In Fig. 3.17 we assumed that the feedback capacitance of (A_1) as well as stray capacitance from gate to ground is zero. In Fig. 3.18, $C_{stray} = 0.37$ pF, and the feedback capacitance of A_1, $C_{GD} = 0.13$ pF. The calculated results of Fig. 3.18 compare quite closely to the actual measurements on receiver #3 shown in Fig. 3.16. In receiver #1, the phase margin was so small that oscillation took place in the closed-loop condition. In order to still use that receiver

RCVR	Voltage Gain	f-3dB of Voltage Gain Section	Amplifier Input Capacitance	e_n $V\sqrt{Hz}^{-1}$	RF Ω	Open Loop f-3dB	APD Dark current at bias	APD Capacitance at bias	Closed Loop f-3dB
1	380	$9x10^6$	5pF	$5x10^{-9}$	$6.12x10^6$	42KHz	$8x10^{-10}$A@10V	0.3pF @10V	6.9MHz
2	390	$8x10^6$	2pF	$22x10^{-9}$	$19.6x10^6$	25KHz		0.3pF @10V	
3	250	$8.5x10^6$	2pF	$22x10^{-9}$	$12.4x10^6$	32KHz	$4.85x10^{-8}$ A@12V	1.5pF @10V	6.35MHz

TABLE I

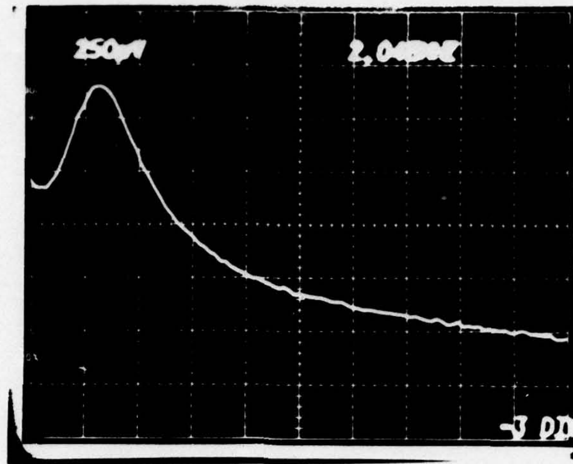

(a)

(b)

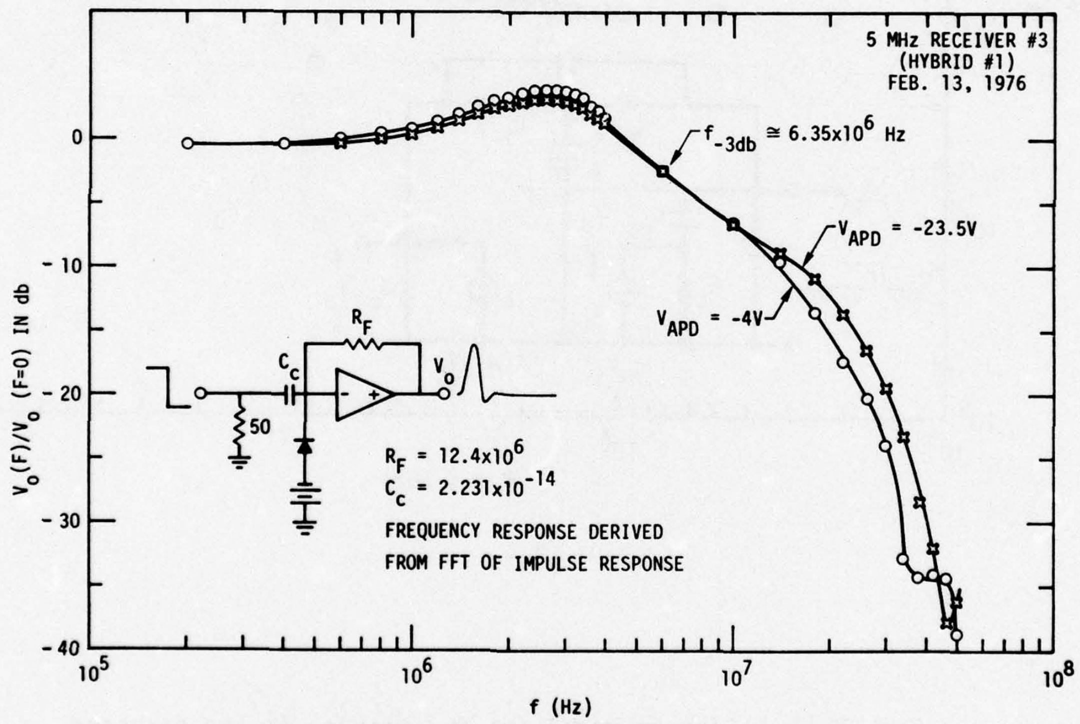

Fig. 3.16. Measured amplitude vs. frequency response for receiver #3 as determined by taking FFT of the impulse response. (a) Direct output of the DPO on linear axes and (b) corrected to logarithmic axes.

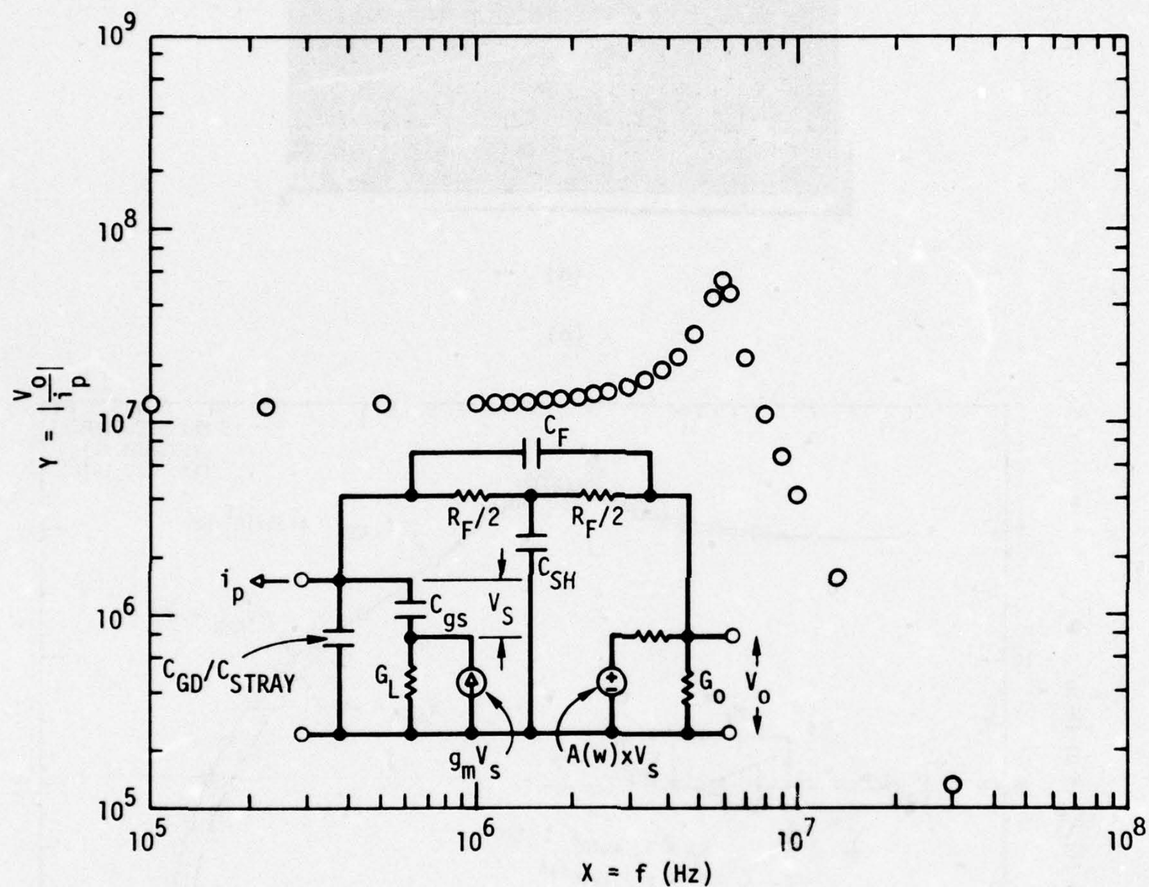

Fig. 3.17. Circuit model showing peaking in the passband.

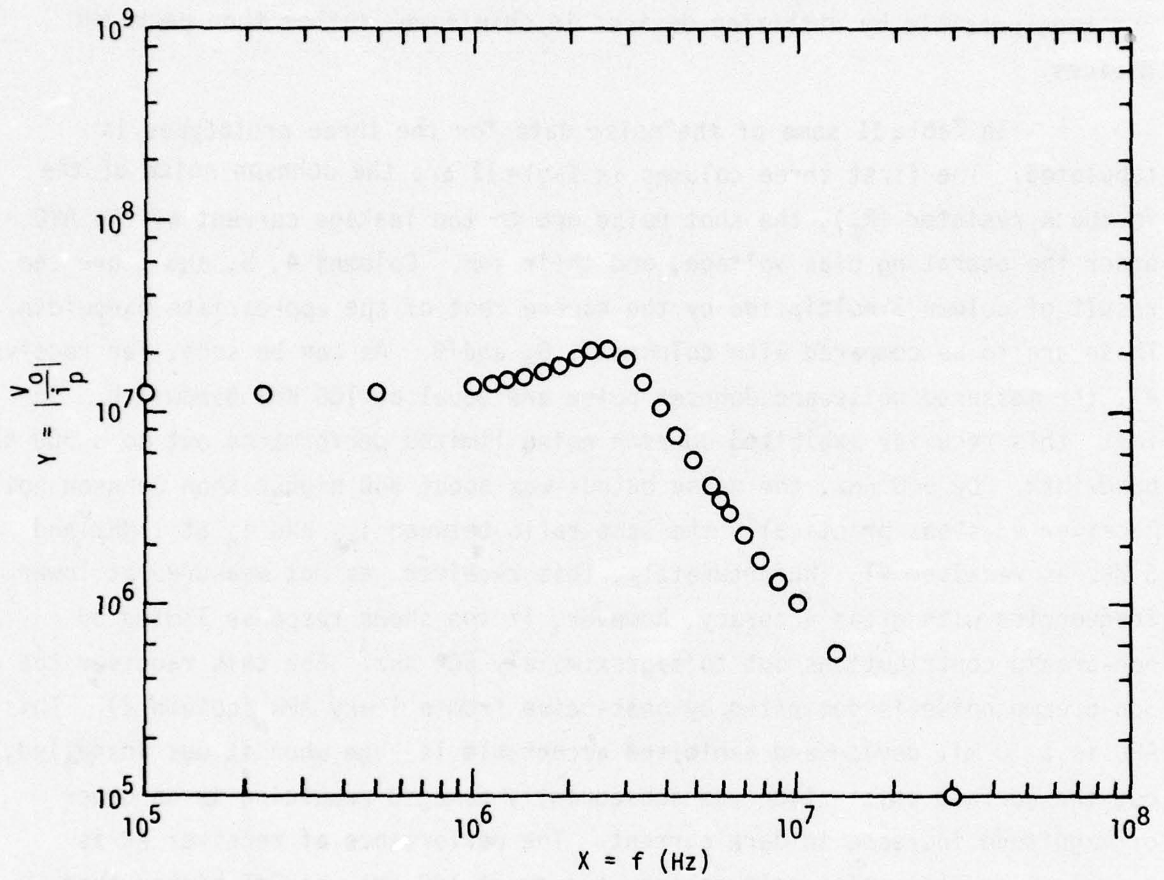

Fig. 3.18. Magnitude of transimpedance of Receiver #3 vs. frequency.

for noise measurements, the feedback voltage was divided by two. This was the easiest thing to do at the time and resulted in enough phase-margin to stabilize the response. Number 3 receiver (the first totally hybrid design) showed the largest phase-margin. This is due to the superior circuit lay-out made possible by utilizing devices in chip form, rather than packaged devices.

In Table II some of the noise data for the three prototypes is tabulated. The first three columns in Table II are the Johnson noise of the feedback resistor (R_F), the shot noise due to the leakage current of the APD under the operating bias voltage, and their sum. Columns 4, 5, and 6 are the result of column 3 multiplied by the square root of the appropriate bandwidth. These are to be compared with columns 7, 8, and 9. As can be seen, for receiver #1, the measured noise and Johnson noise are equal at 100 KHz bandwidth. In fact, this receiver exhibited Johnson noise limited performance out to a 300 KHz bandwidth. By 500 KHz, the noise output was about 3dB higher than Johnson noise. Receiver #3 shows practically the same ratio between i_{nj} and i_n at 1 MHz and 5 MHz as receiver #1. Unfortunately, this receiver was not measured at lower frequencies with great accuracy, however, it too shows response limted by non-preamp contributions out to approximately 500 KHz. For this receiver the non-preamp noise is dominated by shot-noise from a leaky APD (column 2). This APD is a 10 mil device and exhibited acceptable leakage when it was installed, but the surface passivation was subsequently damaged resulting in an order of magnitude increase in dark current. The performance of receiver #2 is anomalous and the noise voltage output even at 100 KHz was 7dB higher than expected. Much more can be learned about the receiver performance by studying the shape of the output noise voltage ($\simeq i_n R_o$) vs. frequency and comparing with the model described earlier.

Fig. 3.19 shows a plot of noise output in $V/\sqrt{Hz}$ for receiver #3 as measured by spectrum analyzer. The feature at 20 MHz in the data has not yet

	EXPECTED NOISE CURRENT DENSITIES			EXPECTED TOTAL i_n			MEASURED i_n DUE TO SHOT, THERMAL, PREAMP			MEASURED $V_n (\propto i_n R_o)$	
RCVR	i_{nj} $A/\sqrt{Hz}$	i_{ns} $A/\sqrt{Hz}$	$i_n = \sqrt{i_{nj}^2 + i_{ns}^2}$ $A/\sqrt{Hz}$	ΔF=100kHz A	1 MHz A	5 MHz A	100 kHz A	1 MHz A	5 MHz A	1 MHz mV	5 MHz mV
1	5.159×10^{-14}	2.2×10^{-14}	5.2×10^{-14}	1.12×10^{-11}	5.2×10^{-11}	11.2×10^{-11}	$\sim 1 \times 10^{-11}$	8.9×10^{-11}	44.4×10^{-11}	0.94	4.62
2	2.90×10^{-14}	1.38×10^{-14}	3.21×10^{-14}	1.01×10^{-11}	3.21×10^{-11}	7.18×10^{-11}	2.3×10^{-11}	29.1×10^{-11}	72.5×10^{-11}	5.7	14.2
3	3.625×10^{-14}	15.89×10^{-14}	16.3×10^{-14}	5.15×10^{-11}	16.3×10^{-11}	36.4×10^{-11}	3.83×10^{-11}	20.2×10^{-11}	107×10^{-11}	0.4	2.12

TABLE II

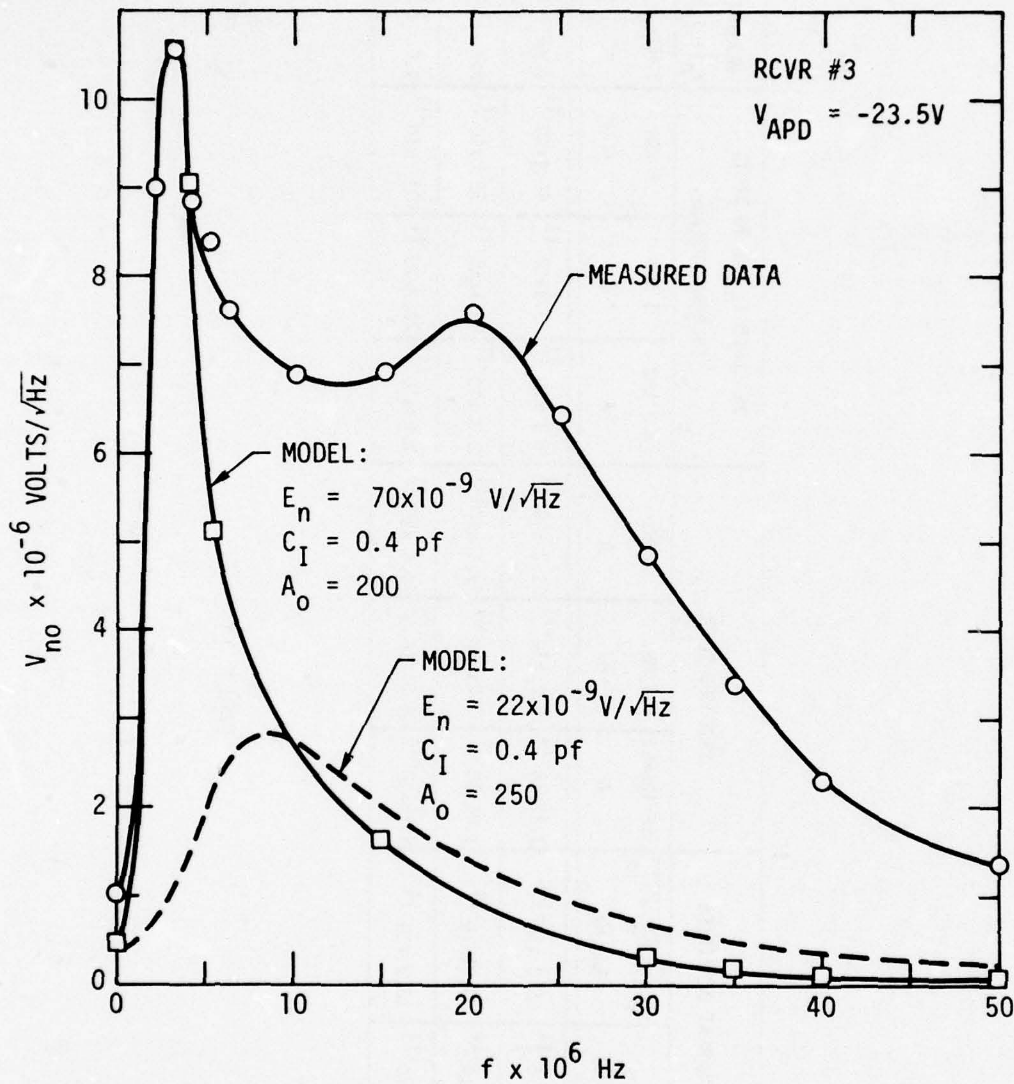

Fig. 3.19 Comparison of measured output noise voltage spectral density vs. frequency with various predictions of noise model for receiver #3.

been analyzed, however, it is of little practical interest since it occurs considerably outside the band of interest (0 to 5 MHz). The dashed curve is the curve calculated from the noise model when the nominal parameter values for this receiver are used. The peak noise predicted occurs at a higher frequency than observation and is about one-third the magnitude of the measured value. One reason for this is apparent when the magnitude of the transimpedance vs. frequency, as predicted by the model is compared with the actual response. Fig. 3.16 b) is the actual response which shows a prominant peak at about 2.6 MHz, the same frequency at which the peak in noise occurs, while the predicted response shows no resonance at all. This is because the model used for the noise analysis does not account for the input circuit of amplifier A_1 in detail as does the model of Fig. 3.17. For purposes of comparison of noise spectra, however, we can adjust the open loop f_{-3dB} of A_0 and the value of C_F (see Figs. 3.9, 10 or 11) in the computer program for the noise model, to create a peak in the magnitude of the transimpedance (and the noise spectrum) which aligns with the measured values. This allows us to account for the added noise due to the peaking of the frequency response but still does not account for the $10.6\mu V/\sqrt{Hz}$ noise voltage peak at 2.6 MHz (Fig. 3.19). This probably represents the limit of applicability of the noise model. This model assumes a noise voltage generator (e_1 in Fig. 3.10) which acts on G_I (the input conductance) to produce a preamp noise term $\propto e_1 G_I f$.

Now, amplifier A_1 is a Mosfet connected in the source-follower configuration, so that its effective input capacitance is $C_{gs}(1-A) \simeq 0.02\ C_{gs} \equiv C_I$. C_{gs} is formed by the actual gate to source capacitance in parallel with C_{APD}, so that the preamp noise term is $e_1\ C_I\ \omega$, (i.e. e_1 multiplies the reduced capacitance rather than the actual capacitance). If the input amplifier has an equivalent input current noise source as well, then the voltage noise induced by this generator would multiply C_{gs} directly, and would produce a noise term that is $e_3\ C_{gs}\ \omega$. In fact, if we increase e_n to $70\times10^{-9} V/\sqrt{Hz}$ in the program, we get the fit shown in Fig. 3.19.

Fig. 3.20 shows the results of the noise spectral comparison on receiver #1. On this receiver, the peaking in the bandpass was eliminated as

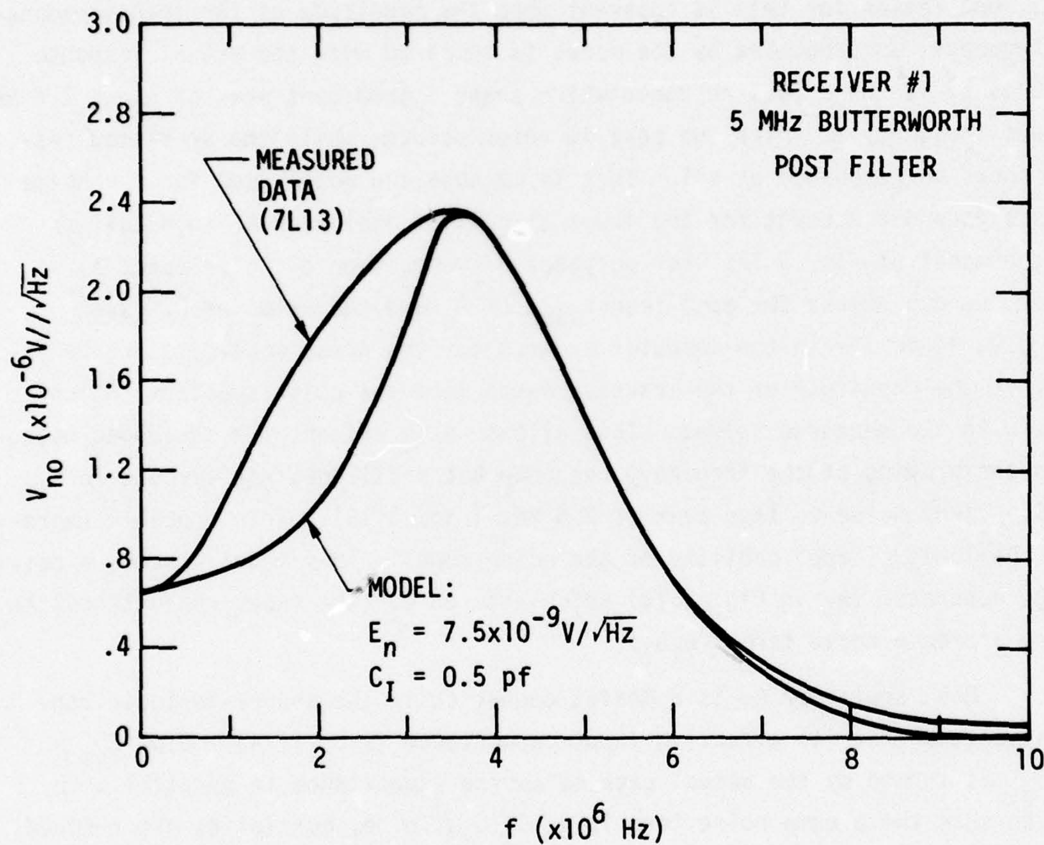

Fig. 3.20 Comparison of measured output noise voltage spectral density vs. frequency with various predictions of noise model for receiver #1.

discussed before and the agreement with the model is better. Here (Fig. 3.20) the data is shown as measured through a 5 MHz Butterworth low-pass filter (with 37 dB/oct. roll-off). The dotted curve is the prediction of the model with the nominal receiver parameters. Again, by artifically shifting the f_{3dB} of A_o, and adjusting e_n to $7.5 \times 10^{-9} V/\sqrt{Hz}$ we get a good fit at the peak of the spectrum. If this computed spectrum (Fig. 3.20) is now integrated, to find the total noise in a 5 MHz bandwidth, we get 3.506 mV. This is to be compared with the 4.62 mV measured result (Table II). The difference comes from the poor fit obtained in the frequency range of 500 KHz to 3 MHz. This lack of fit at low frequencies is probably due to `1/f´ type noise.

Finally, receiver #1 was compared directly with a selected S-1 photomultiplier (ITT, $\eta_{1.06\mu} = 0.1\%$) and GE "Laser-Eye" silicon avalanche photodiode coupled to a 50Ω preamp. Both these devices are commercially available. Table III shows some of the results of this comparison. As can be seen, the S-1 photomultiplier is totally out of consideration, and in the 1 MHz bandwidth the silicon avalanche photodiode is less sensitive by over a factor of 2. Of course, in smaller bandwidths, the difference is even greater.

3.2 Double Heterojunction Photocathode

The goal of this portion of the program is to complete development of a double heterojunction structure and demonstrate field-assisted photoemission into vacuum. In an earlier report(1) (contract no. F33615-75-C-1037) we described the device physics, our Cs activation chamber and the heterojunction device growth and processing steps in considerable detail. Since most of this is unchanged, it will not be repeated in this report. The two areas in which major progress has occured are in fabricating a device structure which will withstand the Cs activation environment and in the actual Cs activation of heterojunction devices (particularly where sputtering is required in the surface cleaning).

	Dark NEP in 1MHz Bandwidth $W/\sqrt{HZ}$	NEP With Light $W/\sqrt{HZ}$	
ITT S-1 Photomultiplier	$2.2x10^{-12}$	$4x10^{-12}$ (P_1=11.5nw)	
GE Silicon ADD/50Ω preamp receiver	$2x10^{-13}$	$7.5x10^{-13}$ (P_1=25nw)	
Science Center GaAsSb photodiode receiver	$9.2x10^{-14}$	$1.16x10^{-13}$ P_1=11.5nw	$2.3x10^{-13}$ P_1=25nw

Table III

The heterojunction photocathode consists of a GaAs emitter (E), a $Ga_{.68}Al_{.32}As$ hole barrier (HB) and a $GaAs_{.86}Sb_{.14}$ absorber (A). An energy band diagram illustrating the principles of operation for this device is shown in Fig. 3.21. This energy band diagram is drawn assuming no "abrupt discontinuities" in the energy bands at the heterojunction interfaces. Fig. 3.21 a) shows the energy bands with no applied bias voltage. It shows a large "potential well" for electrons in the hole barrier region. As bias voltage is applied across the emitter-absorber (the polarity is positive to the emitter so that the absorber-hole barrier junction is reverse biased), the depletion region increases in width across the hole barrier until it just reaches the emitter. At this point, the hole barrier layer is completely depleted (identical to the "punch-through" condition in a PNP transistor) and no electron "potential well" remains in the conduction band. This is shown in Fig. 3.21 b). The device in Fig. 3.21 b) operates as a reflective photocathode (i.e. photons incident and electrons emitted at the same surface). The photons incident on the device pass through the transparent (wide bandgap) emitter and hole-barrier layers to reach the narrow gap absorber where a photoelectron is created in the conduction band. These photoelectrons now have a "down hill slide" (via drift and diffusion) across the hole barrier and emitter layers to the Negative Electron Affinity (NEA) surface where they are emitted into vacuum. The hole bias current remains low on this device because there is still a significant (approximately 0.40 eV) potential barrier in the valence band at the emitter hole barrier junction. This barrier prevents the injection of holes from the emitter into the hole barrier. The proper selection of bias voltage, doping level and energy bandgap of all three layers make it possible to achieve the monitonically decreasing conduction band profile proceeding from the absorber all the way to the vacuum level as shown in Fig. 3.21 b). This condition is necessary for the unimpeded transport of thermalized electrons from the absorber through the emitter and into vacuum.

The major constraint in actually fabricating the above type of photocathode device is that this particular structure can only be grown in one

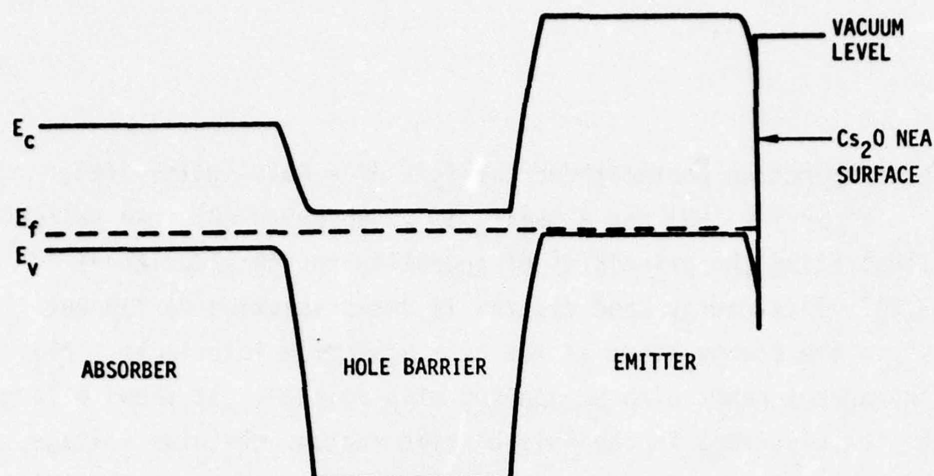

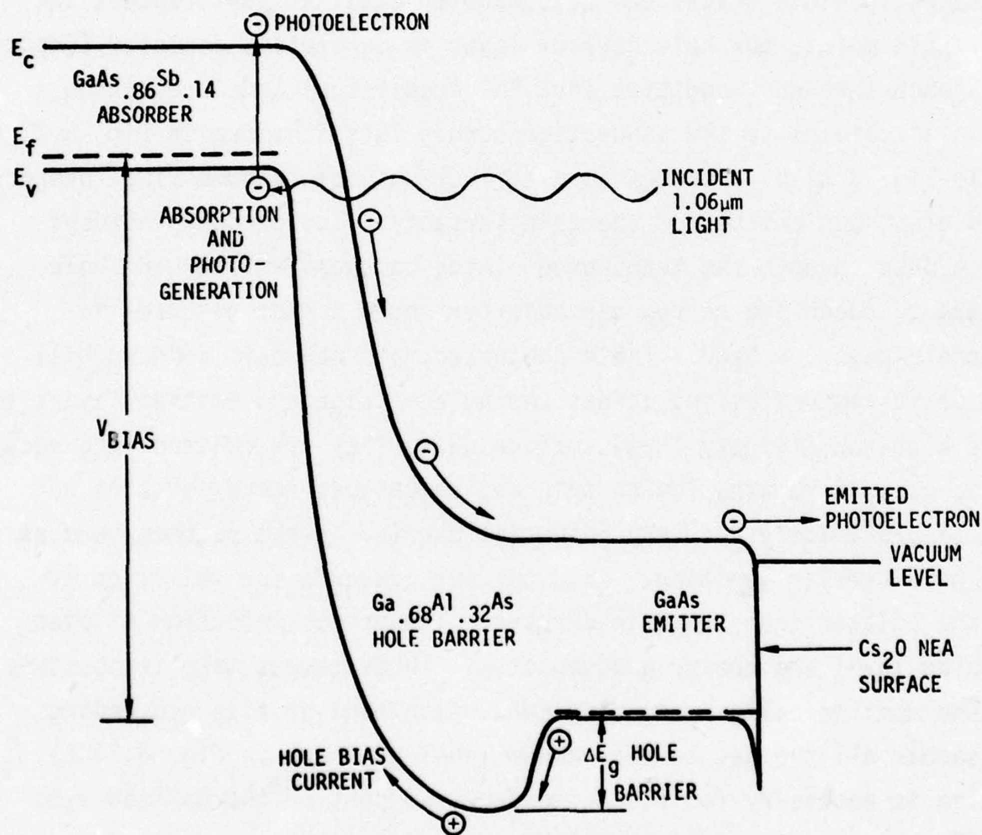

Fig. 3.21 Energy band diagram for the 1.06μm heterojunction photocathode assuming graded junctions with no "abrupt discontinuities." (a) the p-n-p device at zero bias. (b) The p-n-p device biased to "punch through" under operating conditions showing no barrier in the conduction band and ~ 0.4 eV barrier in the valence band.

direction by liquid phase epitaxy: emitter first, then hole barrier, and finally absorber. This problem was discussed in detail in earlier reports[1-2]. This constraint on growth direction is because GaAsSb etches back severely when GaAs or GaAlAs are grown over it, thus destroying the A-HB junction. GaAsSb does, however, grow very readily on GaAlAs or GaAs. Hence, the required photocathode structure can be grown, but the emitter surface requiring Cs activation is buried at the substrate-emitter layer interface in the "as grown" structure. This growth limitation requires the removal of the substrate over any area that will be part of the active device to expose the emitter for Cs activation.

The device structure which we had previously tried to process and activate is shown in Figs. 3.22 and 3.23. Fig. 3.22 shows the various layers (including chemical composition, dopants and their concentration and thickness) required for the photocathode. This structure shows two layers in addition to the E-HB-A required for the photocathode. The first of these layers is a Sn doped n-GaAs layer to use in the substrate removal process, a selective electrochemical etching technique which etches p-GaAs but not n-GaAs, hence the designation of etch stop (ES) layer. The second layer is Ge doped p^+-GaAs which prevents Zn diffusion from the heavily Zn doped GaAs substrate up into the ES layer and is thus a diffusion barrier (DB) layer. The actual device configuration is shown in Fig. 3.23 where the initial structure (Fig. 3.22) is mounted on a ceramic substrate with openings to the substrate. The substrate and DB have been removed by selective electrochemical etch and the ES by chemical etch to expose the emitter surface for activation.

Devices of this type (Fig. 3.23) were fabricated, however, the very thin active device region proved to be a serious problem. Many of the devices broke near the end of the etch thinning process or in the final surface cleaning before activation. Those few devices which survived the processing did not survive heat cleaning in the activation chamber. This breakage from sample heating was always at the outer edges of the device just where it joined the thicker substrate region. The thin active region has a much lower thermal mass

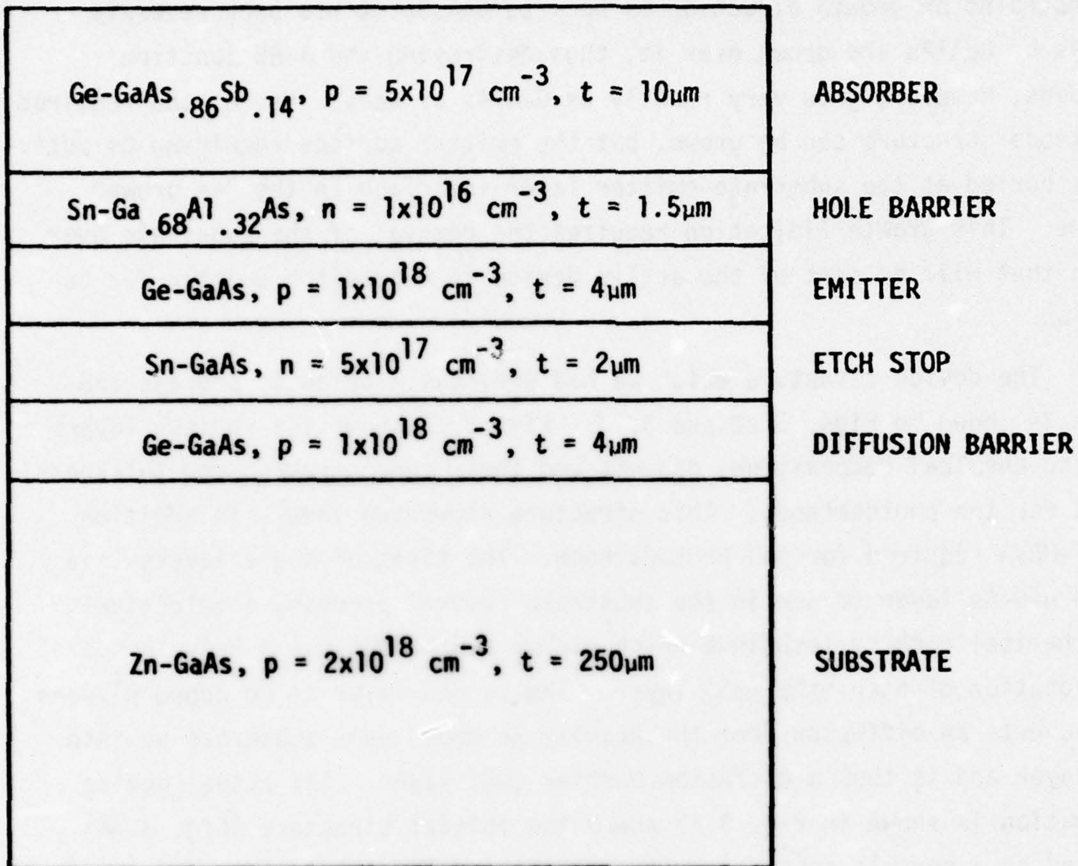

Fig. 3.22 **Schematic diagram of the double heterojunction photocathode structure for activation. The thickness, chemical composition, dopant and carrier concentration for each layer is also shown in the diagram.**

and much higher thermal resistance to any heat sink. Since the device is heated radiatively by a lamp in the chamber, it heats much faster than the substrate. This large thermal stress in such a thin region (~ 15μm) always resulted in breakage.

The solution to this problem is to fabricate a device structure in which the thin active region of the device is structurally supported by a material with a good thermal expansion match to the heterojunction photocathode. Such a device structure has been designed [2] and the techniques to process and activate this structure are described in this report.

3.2.1 Device Processing

As described above, our first photocathode structure was very fragile and could not withstand the thermal stresses created during heat cleaning. The solution to this problem is to fabricate a device structure in which the thin active region of the device is structurally supported by a substrate with a good thermal expansion match to the device to eliminate both the breakage and thermal stress problems.

A device structure which fulfills the above requirements is shown in Fig. 3.24. This device utilizes the same initial structure shown in Fig. 3.22. The photocathode device structure is, however, significantly different than that in Fig. 3.23. In the new device structure, the "as grown" structure is bonded to a second GaAs substrate with the absorber down. The original growth substrate is removed by exactly the same combination of lapping, chemical and electrochemical etching as used previously, except the entire substrate is removed rather than just the area exposed through the holes in the ceramic support. This new device is completely supported by the second GaAs substrate which provides both the necessary physical support and a good thermal expansion match to the device.

Since most of the processing in the present device is identical to our earlier device, the processing is just summarized and the reader is referred

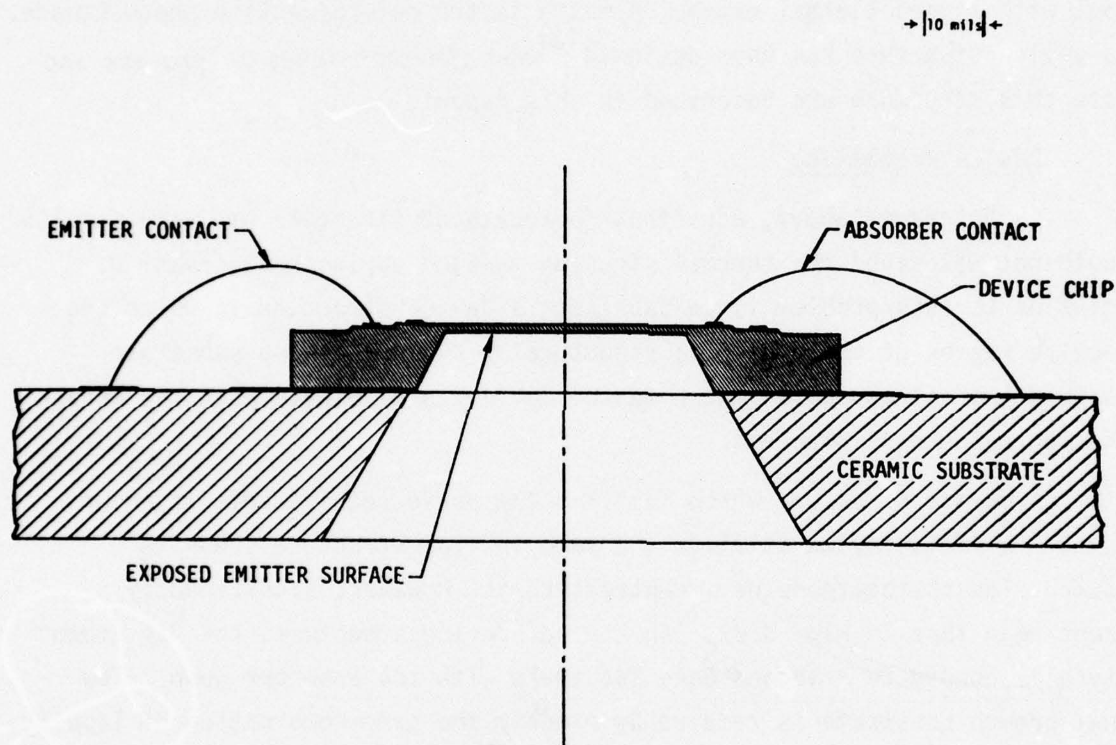

Fig. 3.23 Schematic diagram of the double heterojunction photocathode showing the planned mounting, bonding and substrate removal required to produce a device for Cs activation.

to our earlier report[2] for specific details in the processing.

A cross-sectional diagram of the "as grown" structure is shown in Fig. 3.22. The photocathode device is fabricated in the following sequence:

1) The absorber surface of the sample is polished to obtain a perfectly flat surface.

2) Layers of W, Ti and Au are sequentially sputter deposited on the absorber. The thicknesses are about: 2000Å-W, 500Å-Ti, 2u-Au.

3) The sample is eutectically bonded, with the absorber down, to a second piece of GaAs substrate material which will become the new mechanical support. A cross-sectional view of the device at this point is shown in Fig. 3.24.

4) The original p^+ - GaAs substrate is removed from the entire area of the sample by a sequence of polishing, chemical, and electrochemical etching. The technique used to remove the last part of the GaAs substrate is a selective electrochemical etch in KOH which etches the p^+ - GaAs, but stops at the n - GaAs etch stop (ES) layer. The ES layer is removed after the device mesa etch thus minimizing the exposure of the emitter surface prior to activation.

5) The device mesa is defined using a photoresist method.

6) The device mesa is etched in H_2O_2: NH_4OH:H_2O until the E and HB layers have been removed.

7) The sample is cleaned to remove the photoresist.

8) The n^- GaAs (ES) layer is etched in H_2O_2: NH_4OH:H_2O until the ES layer is completely removed and ~ 1μm of the emitter is also removed. This absolutely insures that the p^+ - GaAs emitter will be exposed for activation.

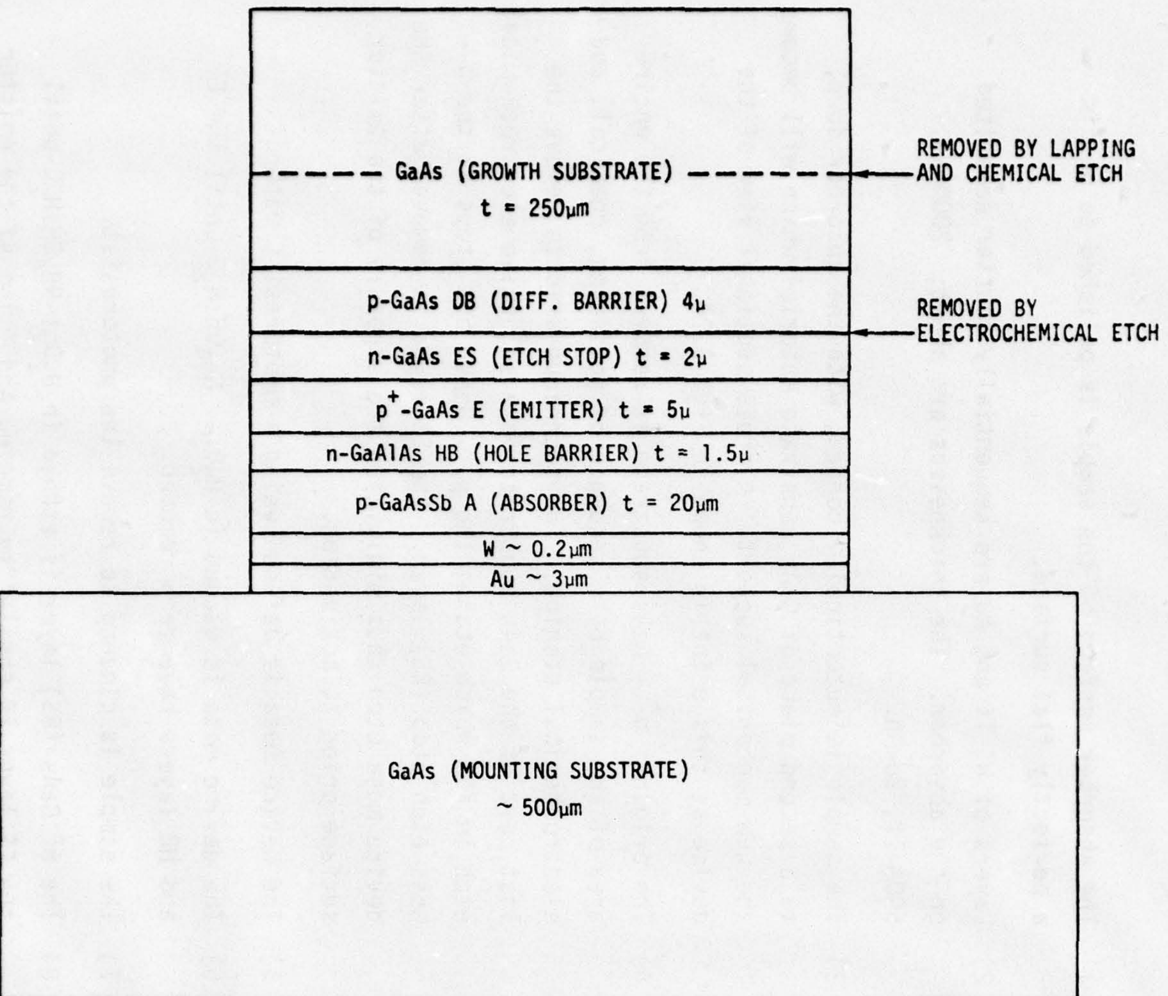

Fig. 3.24 The proposed new device structure in which the epitaxial structure is eutectically bonded, absorber down, to a second GaAs substrate. The original GaAs growth substrate is then selectively removed by a combination of lapping and chemical and electrolytic etching to expose the emitter surface.

9) Ag + Mn alloy is evaporated onto the emitter surface of the device to obtain ohmic contact.

10) A protective W dot is sputter deposited on the surface of the device at the outer perimeter so that it is connected to the Ag-Mn ohmic contact ring.

11) The entire device structure is mounted onto a Mo substrate which is placed on a ceramic holder with a W probe and electrical contacts. The W probe (a 5 mil wire with very little spring tension) is carefully contacted to the W dot on the device perimeter and the entire holder is immediately loaded into the activation chamber.

Several devices, both cold cathodes and photocathodes, have now undergone the complete processing. This new structure is a major improvement over the initial structure and they mechanically withstand the thermal process prior to activation.

3.2.2 Cs Activation

In our prior report[2], we described our Cs activation chamber and our early activation results. Auger and x-ray photoelectron spectroscopy (XPS) measurements on surfaces subjected to the processing described in the previous section suggested that sputter cleaning of the surfaces would be required for Cs activation of active device structures. Thus the major effort has been to develop an activation technique (including sputtering) which would be suitable for heterojunction structures and to successfully activate a heterojunction photocathode.

3.2.2.1 Effect of Cs and O_2 on Photoyield

Although a definitive model of the physics underlying the cesium oxide - GaAs surface interaction that produces NEA is not yet available, an empirical procedure can be established to routinely activate GaAs surfaces to NEA. In this section we describe the cesium deposition and oxidation steps we follow to maximize the photoyield on our GaAs samples.

After cleaning under vacuum to obtain as near to an atomically clean surface as possible (more will be said on this topic in the next section), we position a sample to face the focussed specular white light output (~ ½ mm spot) of a monochromator having a tungsten filament source. Next, the sample surface is exposed to a flux of Cs atoms from a nearby Cs source. The Cs source is valved to allow the Cs flux to be turned on and off quickly. Initially, with no Cs, there is no photocurrent from the sample, the electron affinity of GaAs being 4.05 eV. As the Cs from the source begins to stick to the sample, the electron affinity of the surface decreases, followed at some point by the onset of photoemission. Cesiation is continued until a peak white-light photoemission current is obtained (which is thought to occur at less than a monolayer of Cs coverage). Additional Cs at this juncture decreases the photocurrent. There is no means to quantitatively determine the amount of Cs on the sample surface at a given time, although Auger measurements provide a qualitative measure.

Fig. 3.25 is a series of spectral yield curves (electrons per incident photon vs. wavelength) taken at various times during the activation of a p^+-Ge doped epitaxial layer. The sample was chemically pre-cleaned, then heat cleaned under vacuum. Curve (a) is the spectral yield for the peaked Cs - only step described above. Note that photoemission does occur out to wavelengths around the GaAs bandgap, but with low yield. Letting a controlled amount of O_2 into the chamber through a leak valve forms cesium oxide on the sample surface to further decrease the sample work function, which, in turn, gives the higher spectral yield curve (b) in Fig. 3.25 and a six-fold increase in white light photoemission. Cycles of Cs exposure followed by O_2 exposure are continued until there is no further increase in white light response. The treatment for each curve in Fig. 3.25 is:

Yield Curve	Number of Cs - O_2 Cycles	Relative White-Light Photocurrent
(a)	Cs only	1
(b)	1	6.5
(c)	2	10
(d)	3	12
(e)	10	17

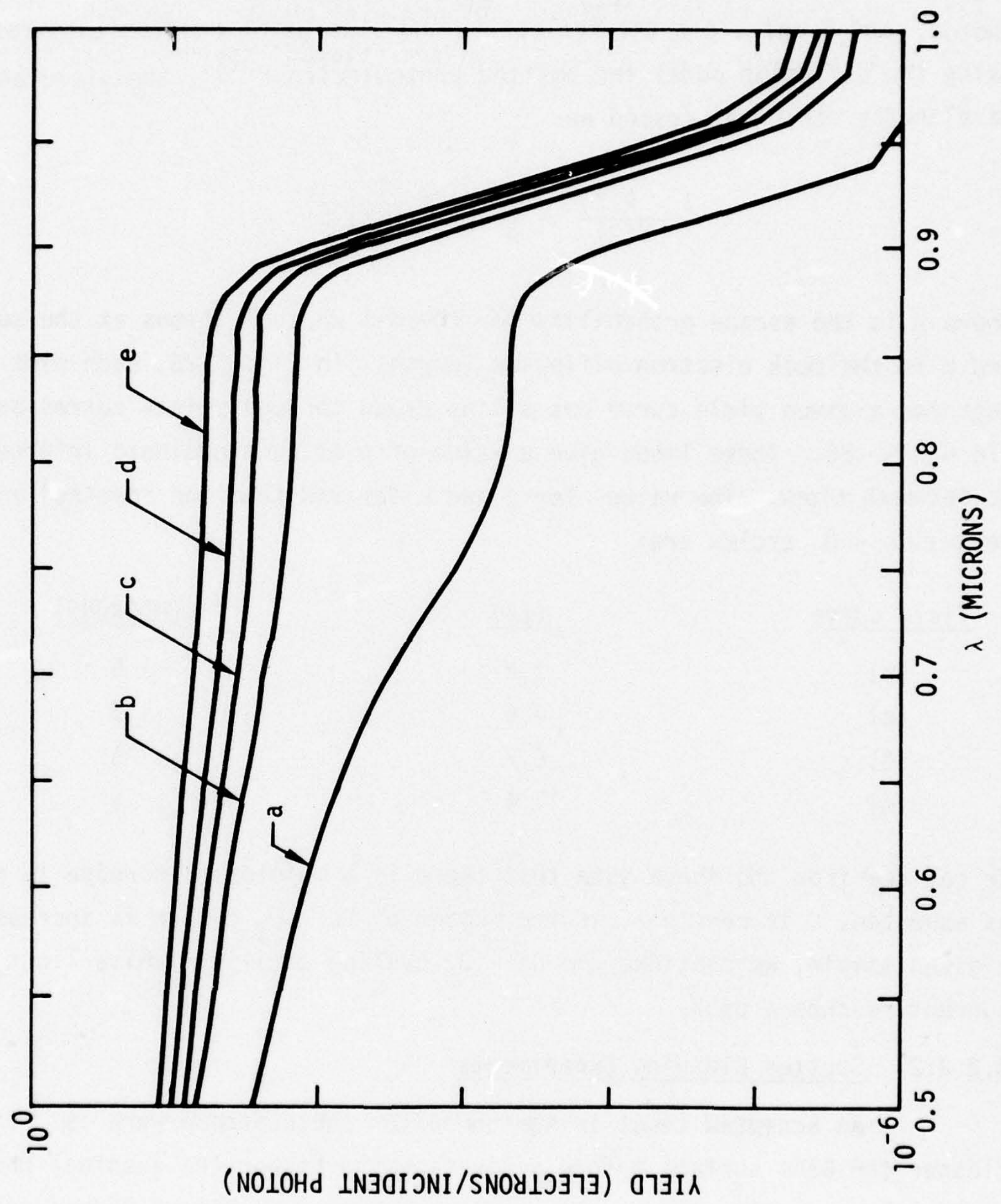

Fig. 3.25 Influence of Cs - O cycles on spectral yield; (a) Cs only; (b) 1 cycle; (c) 2 cycles; (d) 3 cycles; (e) 10 cycles.

Fig. 3.26 has the spectral yield data of curves b, c, d, e in Fig. 3.25 replotted as $\frac{1 - R(\lambda)}{Y(\lambda)}$ vs. $\frac{1}{\alpha(\lambda)}$, where Y is the yield per incident photon, and R and α are the reflection and absorption coefficients respectively. Using the diffusion model for emitted photoelectrons[12], the yield at long wavelengths can be expressed as:

$$\frac{1 - R(\lambda)}{Y(\lambda)} = \frac{1}{p} \left(1 + \frac{1}{\alpha(\lambda) L}\right)$$

Where p is the escape probability for thermal photoelectrons at the surface and L is the bulk electron diffusion length. In Fig. 3.26, each plot of the data for a given yield curve has a line drawn through points corresponding to $.76 \leqslant \lambda \leqslant .86$. These lines give a value of p at each ordinate intercept and pL for each slope. The values for p and L derived from the spectral yields versus Cs - O_2 cycles are:

Yield Curve	p(%)	L(MICRONS)
(b)	2.2	5
(c)	4.6	5
(d)	6.7	5
(e)	11.4	5

We can see from the above data that there is a monotonic increase in p while, as expected, L is constant, as the number of Cs - O_2 cycles is increased. For a given sample, we continue the Cs - O_2 cycling until the white-light photocurrent reaches a peak.

3.2.2.2 Sputter Cleaning Experiments

An accepted tenet in semiconductor photocathode work is: the cleaner the GaAs surface before activation the higher the eventual photoemission yield. For example, the sample used for the data in Fig. 3.25 had enough residual surface C contamination after heat cleaning, as seen by AES, to no doubt be the major factor in limiting the overall yield to ~ 450μ Amps/lumen. As an

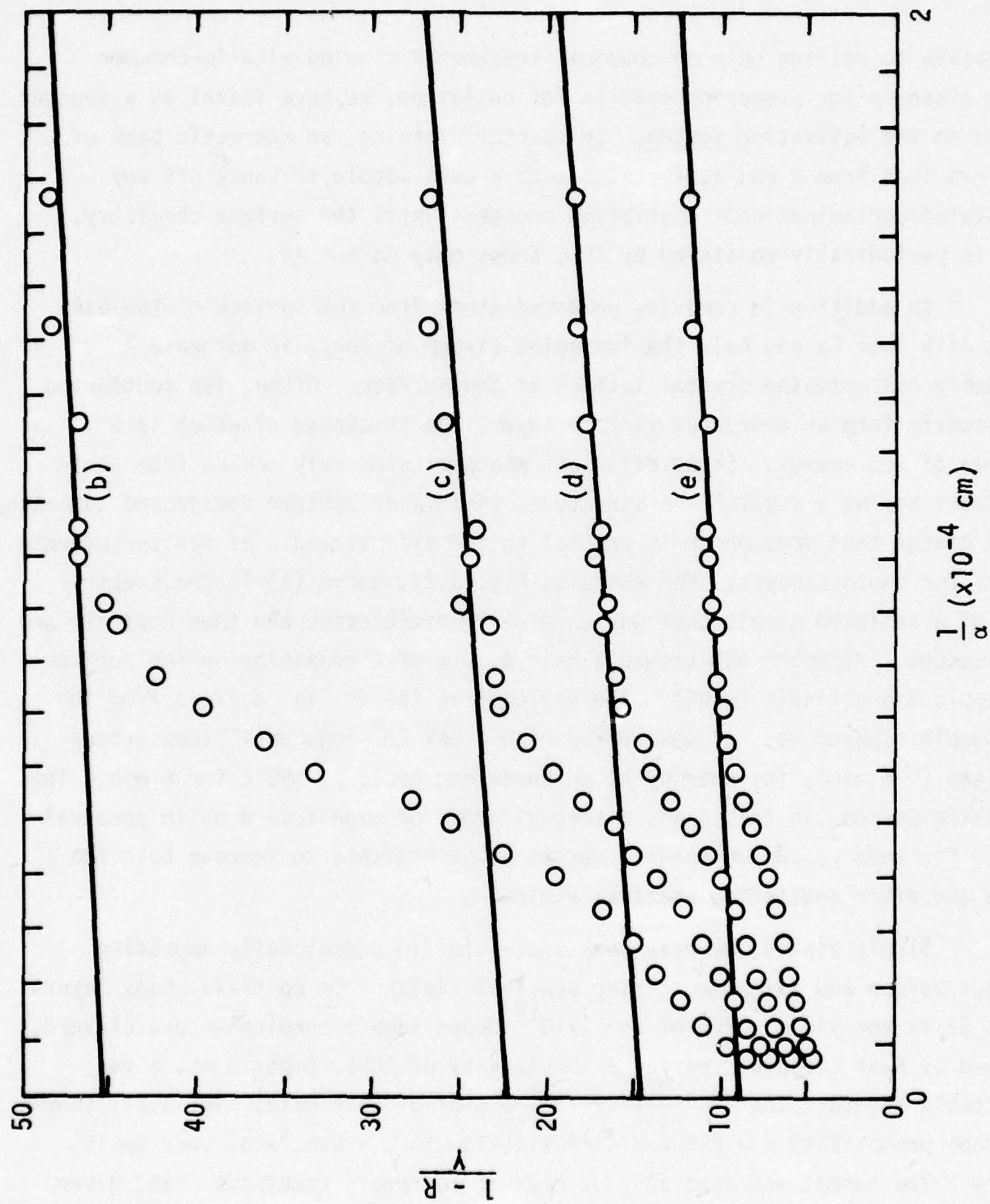

Fig. 3.26 Data in Fig. 3.25 replotted as $\frac{1-R}{\gamma}$ vs. $\frac{1}{\alpha}$.

alternative to relying only on chemical treatments coupled with in-chamber vacuum cleaning for preparing samples for cesiation, we have installed a sputter ion gun on the activation system. In sputter cleaning, an energetic beam of inert gas ions from a gun is focussed onto a GaAs sample to knock off any accumulated contamination. Sputtering proceeds until the surface chemistry, which is periodically monitored by AES, shows only Ga and As.

In addition to removing unwanted atoms from the surface of the GaAs (along with some Ga and As), the impinging stream of ions, in our case Ar^+, inevitably disrupts the crystal lattice at the surface. Often, ion sputtering can actually form an amorphous surface layer, the thickness of which is a function of ion energy. Since efficient photoemission only occurs from semiconductors having a crystalline structure, minimizing sputter damage and annealing out of damage that does occur is crucial to the effective use of sputter-cleaned samples for photocathodes. For example, Fig. 3.27, curve (a) is the spectral yield of a cesiated sample that was chemically pre-cleaned and then heat cleaned under vacuum. Although AES showed a fair degree of C remaining on the surface, the sample did activate to NEA. The yield curve (b) in Fig. 3.27 is from the same sample exposed to: a) sputtering with 1 keV Ar^+ ions until the surface was clean (~ 5 min), followed by b) an annealing cycle of 590°C for 6 min. The sputtering caused, in this case, a several order of magnitude drop in spectral yield. For this reason we began a series of experiments to improve both the before and after sputtering spectral yields.

Simply stated, we have been successful in dramatically improving both our before and after sputtering spectral yields from epitaxial GaAs layers. Fig. 3.28 is the yield curve of a $\sim 1 \times 10^{18}$ doped sample chemically pre-cleaned, followed by heat cleaning, having a sensitivity of 1005μ Amps/lumen, a very respectable figure. The $\frac{1 - R(\lambda)}{Y(\lambda)}$ vs. $\frac{1}{\alpha(\lambda)}$ plot of this data, Fig. 3.29, shows an escape probability $p = 25\%$ and diffusion length $L = 8\mu m$, also very satisfactory. The sample was next sputter cleaned to remove remaining C and given an anneal cycle. Reactivation gave the yield curve in Fig. 3.30, and a sensitivity of 700μ Amps/lumen. The $\frac{1 - R(\lambda)}{Y(\lambda)}$ vs. $\frac{1}{\alpha(L)}$ plot, Fig. 3.31, for the

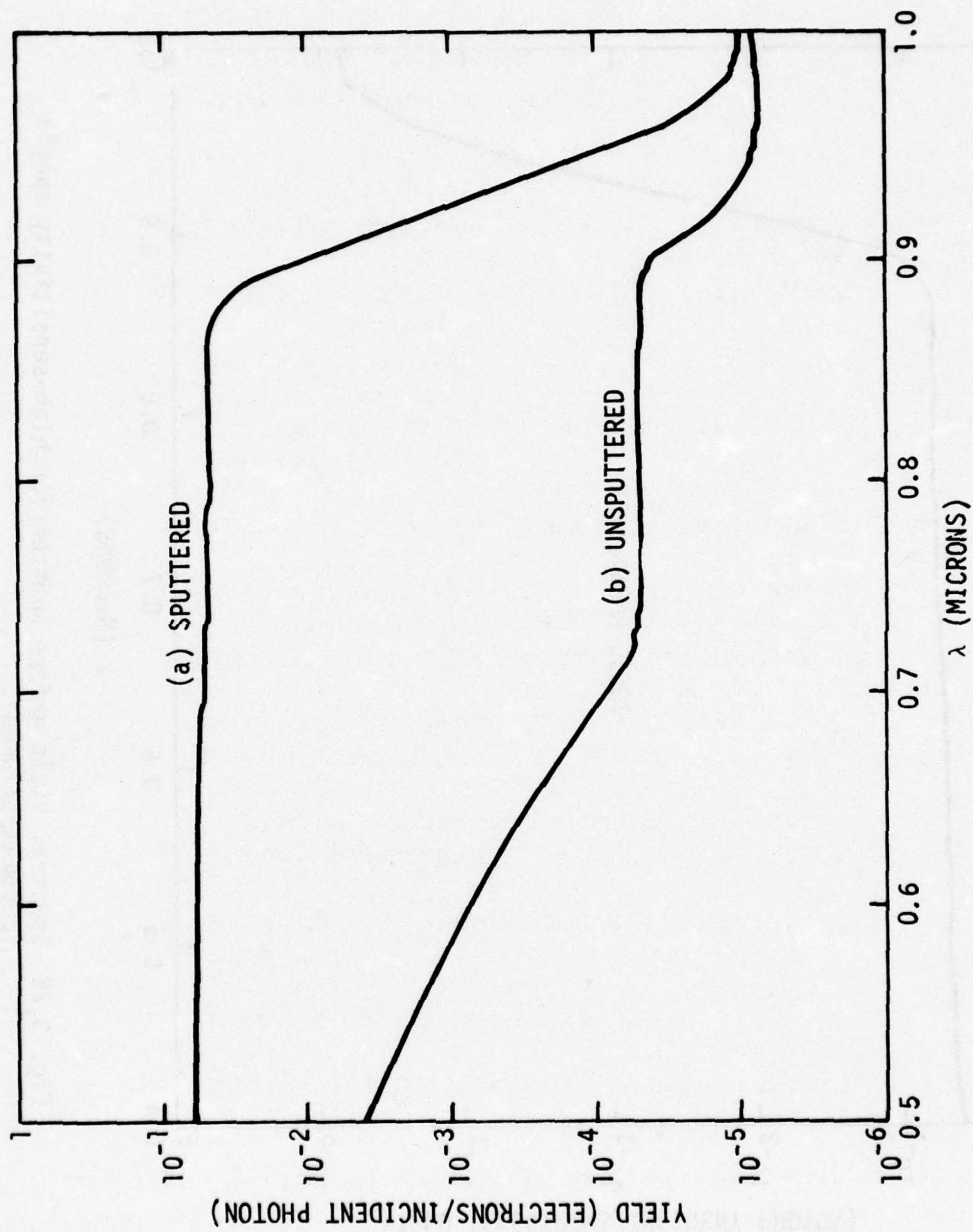

Fig. 3.27 Comparison of spectral yield before and after sputter cleaning with 1 keV Ar^{+} ions and 590°C anneal temperature.

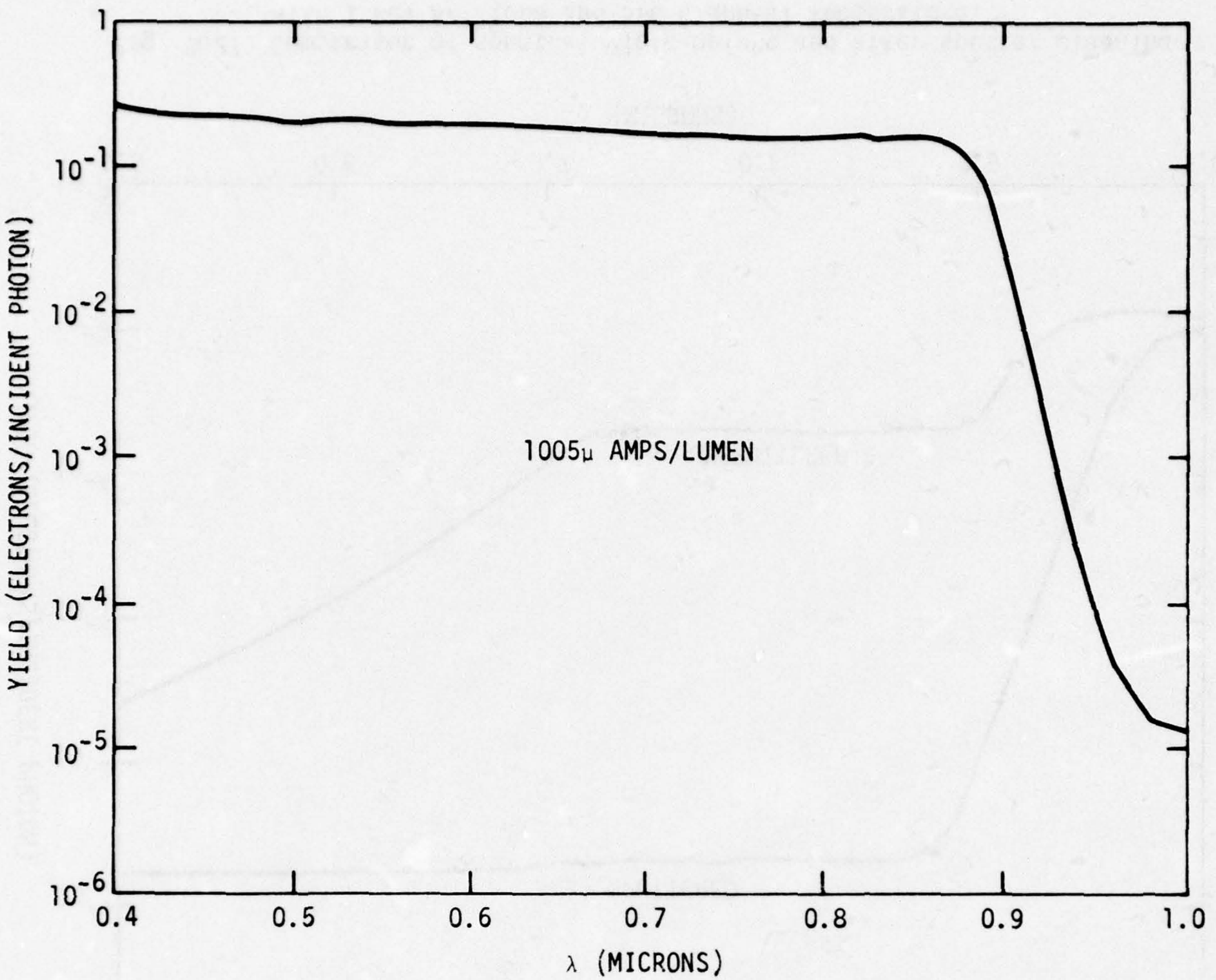

Fig. 3.28 Spectral yield before sputter for high-sensitivity sample (1005μamps/lumen).

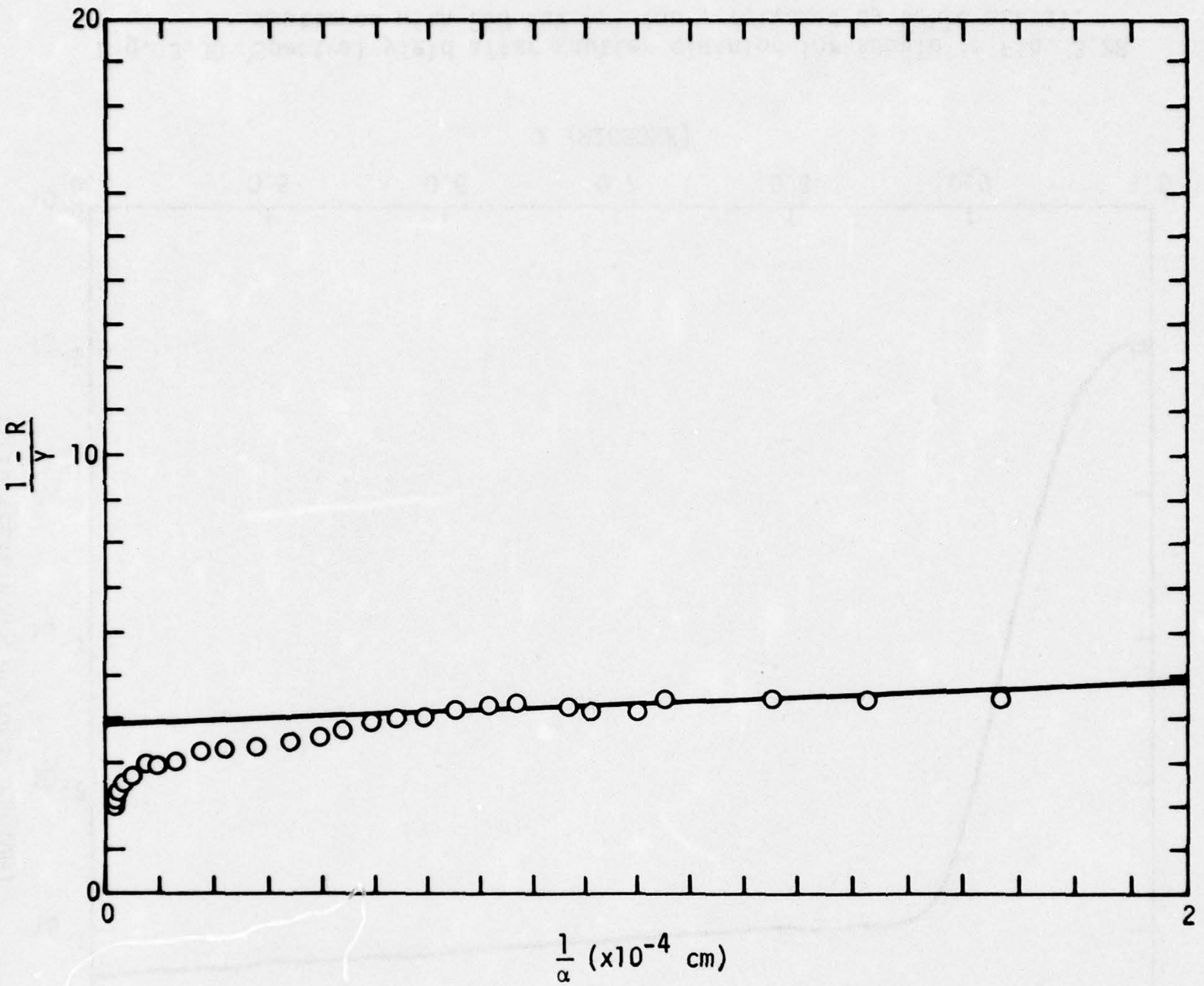

Fig. 3.29 $\frac{1-R}{Y}$ vs. $\frac{1}{\alpha}$ plot for Fig. 3.28 data. $p = 25\%$, $L = 8\mu m$.

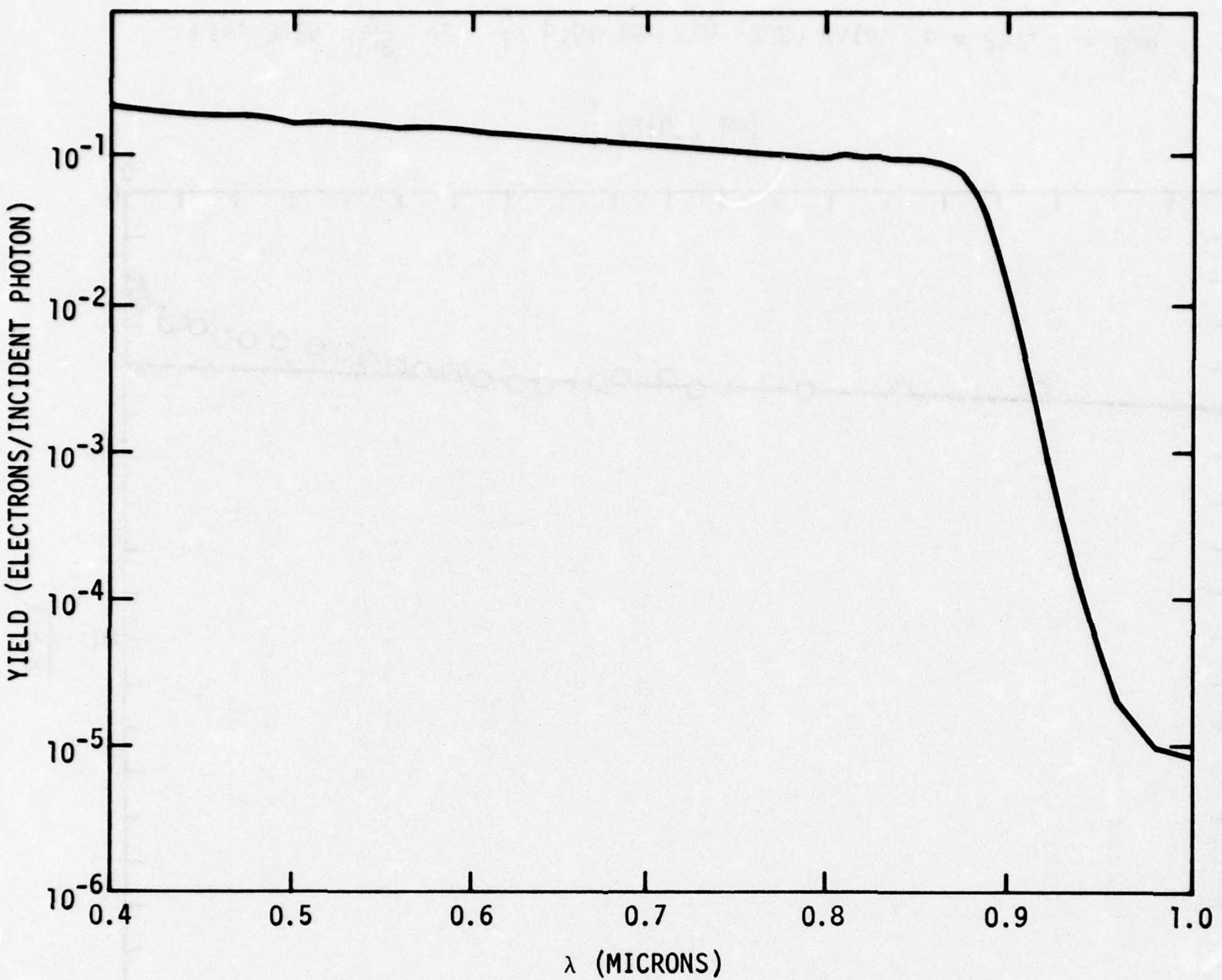

Fig. 3.30 Spectral yield after sputter cleaning for sample in Fig. 3.28 sputtered with 250 keV Ar^+ ions, followed by 605°C anneal.

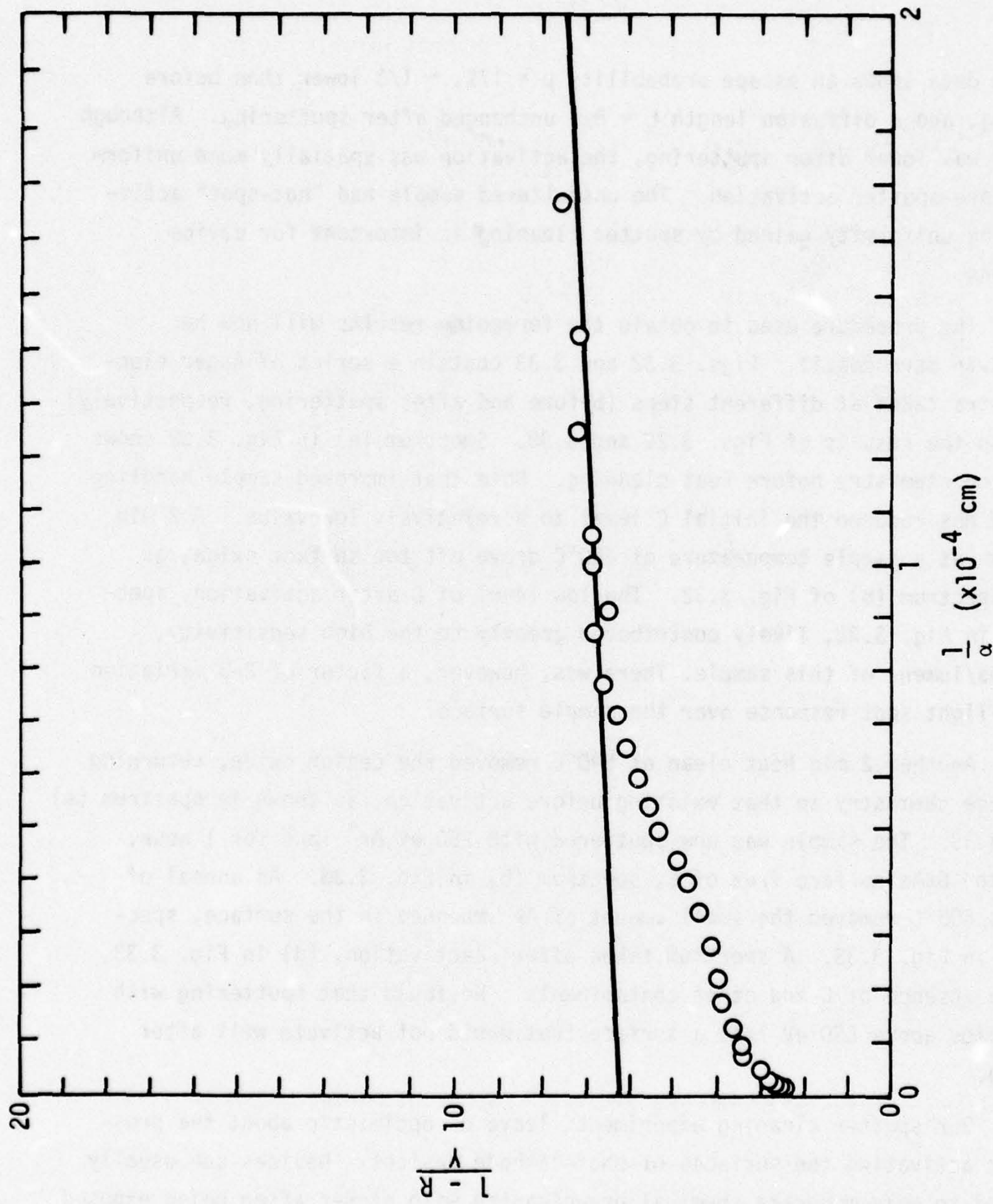

Fig. 3.31 $\frac{1-R}{Y}$ vs. $\frac{1}{\alpha}$ plot for Fig. 3.30 data. p = 17%, L = 8μm.

sputtered data shows an escape probability $p = 17\%$, $\sim 1/3$ lower than before sputtering, and a diffusion length $L = 8\mu$, unchanged after sputtering. Although the yield was lower after sputtering, the activation was spatially more uniform than the pre-sputter activation. The unsputtered sample had "hot-spot" activation. The uniformity gained by sputter cleaning is important for device activations.

The procedure used to obtain the foregoing results will now be described in more detail. Figs. 3.32 and 3.33 contain a series of Auger electron spectra taken at different steps (before and after sputtering, respectively) leading to the results of Figs. 3.29 and 3.30. Spectrum (a) in Fig. 3.32 shows the surface chemistry before heat cleaning. Note that improved sample handling technique has reduced the initial C level to a relatively low value. A 2 min heat clean at a sample temperature of 590°C drove off the surface oxide, as seen in spectrum (b) of Fig. 3.32. The low level of C after activation, spectrum (c) in Fig. 3.32, likely contributed greatly to the high sensitivity, 1005μ Amps/lumen, of this sample. There was, however, a factor of 2-3 variation in white-light spot response over the sample surface.

Another 2 min heat clean at 590°C removed the cesium oxide, returning the surface chemistry to that existing before activation, as shown in spectrum (a) of Fig. 3.33. The sample was now sputtered with 250 eV Ar^+ ions for 1 hour, leaving the GaAs surface free of C, spectrum (b) in Fig. 3.33. An anneal of 30 min at 605°C removed the small amount of Ar imbedded in the surface, spectrum (c) in Fig. 3.33. A spectrum taken after reactivation, (d) in Fig. 3.33, shows the absence of C and other contaminants. We found that sputtering with ion energies above 250 eV left a surface that would not activate well after annealing.

Our sputter cleaning experiments leave us optimistic about the prospects for activating the surfaces of photocathode devices. Devices can usually be exposed to only moderate chemical pre-cleaning with etches after being exposed to the various organic resists and solvents used in fabrication processing. Sputtering with low-energy 250 eV Ar^+ ions can be used to remove the relatively

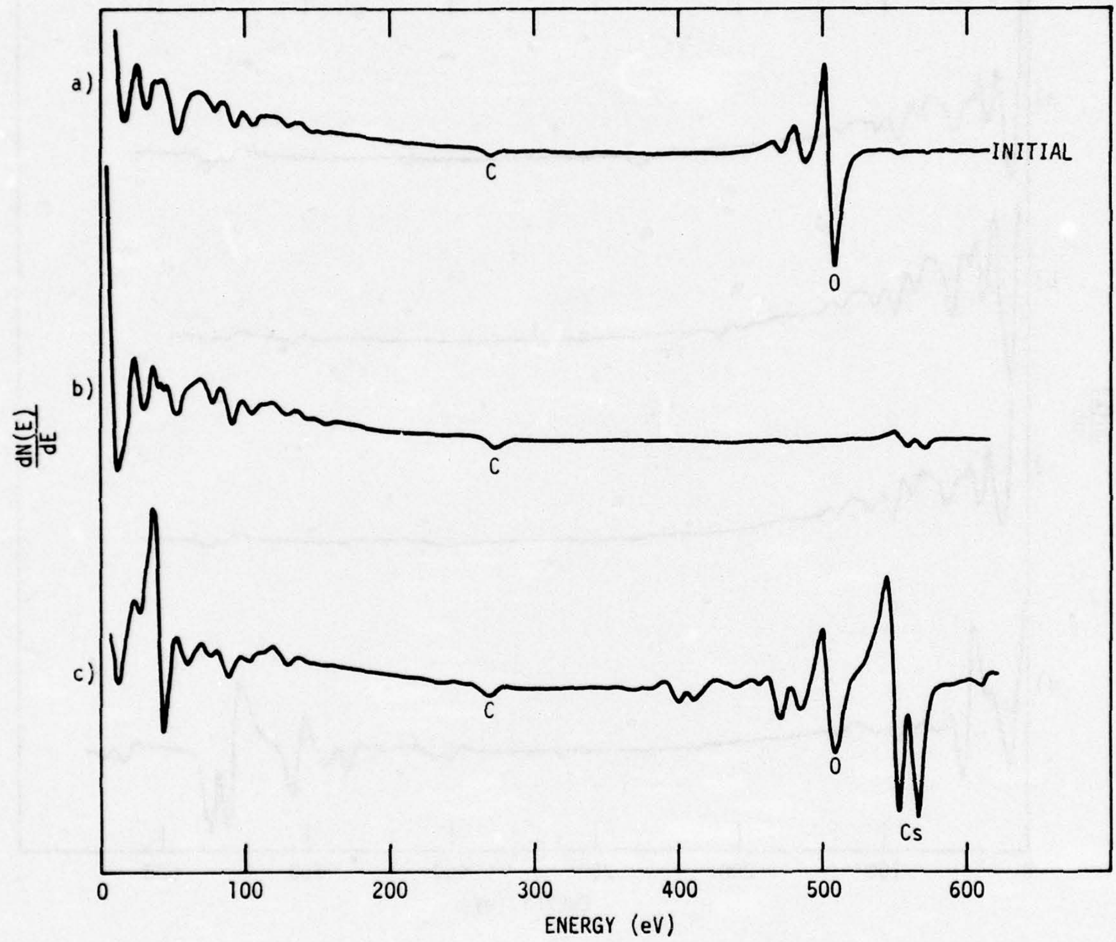

Fig. 3.32 Auger electron spectra before sputtering: (a) initial, before heat cleaning; (b) after heat clean, 2 min at 590°C; (c) after Cs - O activation.

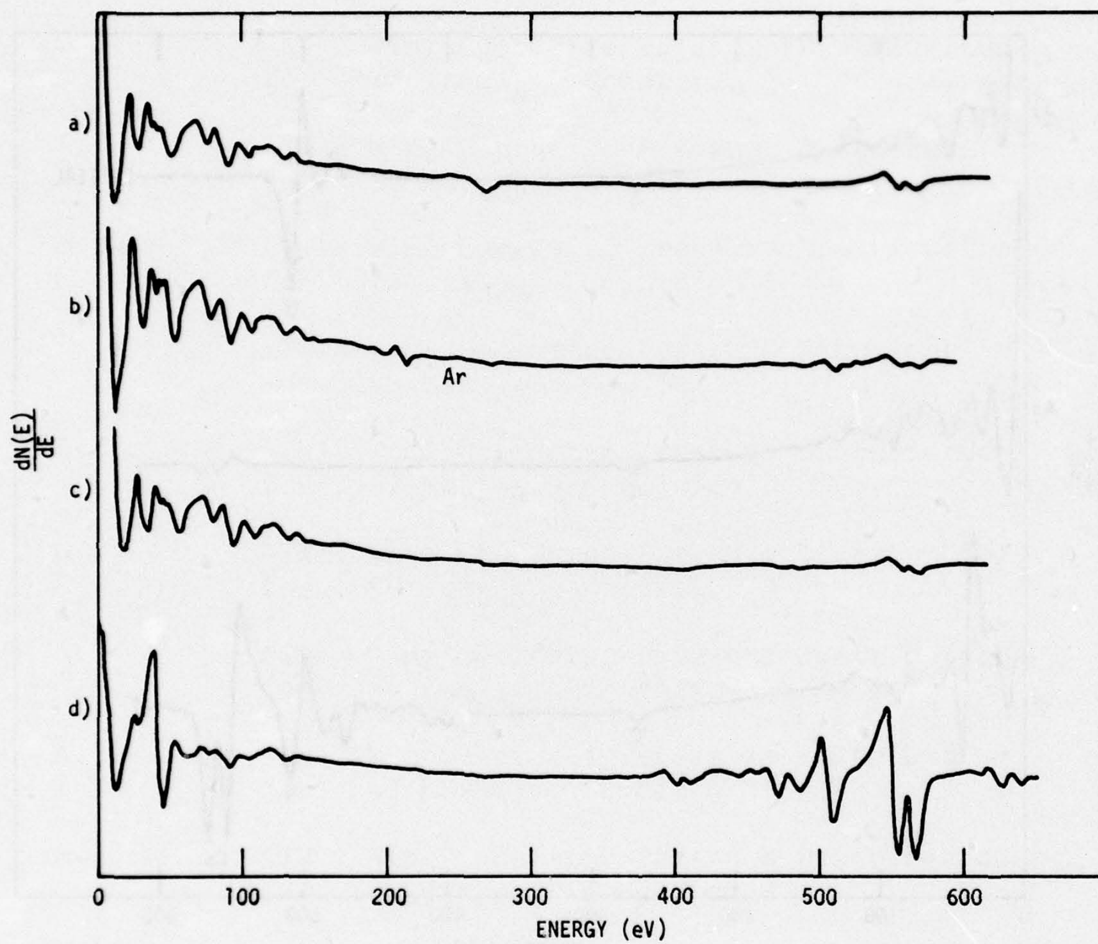

Fig. 3.33 Auger electron spectra after sputtering: (a) initial, before sputtering; (b) after 1 hr. sputter with 250 eV Ar^+ ions; (c) after 30 min anneal at 605°C; (d) after Cs - O activation.

high residual C typically found on devices, leaving a surface that can, with proper annealing, be activated to high spectral yield. Furthermore, we have found the surfaces cleaned by sputtering to have spatially uniform light sensitivity (not true for non-sputtered sample), an important consideration for imaging photocathode devices.

3.2.2.3 Cold Cathode Activation

Because of the complexity of the double heterojunction photocathode, the initial heterojunction device experiments were carried out on a GaAlAs-GaAs "cold cathode". The device structure is shown in Fig. 3.34. This device closely simulates 2/3 of the photocathode because the n-$Ga_{.68}Al_{.32}As$ and p-GaAs are grown of the identical composition, doping densities and thickness as the hole barrier and emitter layers in the 1.06μm photocathode. These devices are mounted in the same fashion as the photocathode, activated and then measured to determine cathode efficiency, success of the Cs activation and its effect on the I-V characteristic of the heterojunction.

The cold cathode device shown in Fig. 3.34 is straightforward to process because the emitter layer is grown last and is exposed for activation "as grown". The processing is similar to the photocathode processing with a Ag-Mn ohmic contact on W dot at the perimeter for the external W probe contact.

After the cold cathode was put into the activation chamber, a series of log I vs. V characteristics were taken at various points in the activation to study the junction behavior. Log I vs. V characteristics provide information on the nature of the diode current (i.e. diffusion, generation-recombination in the depletion region, tunnelling or surface)[13] and thus provide information on the effects of the activation process.

A series of log I vs. V characteristics are shown in Figs. 3.35 through 3.38. These results were obtained on a GaAlAs-GaAs cold cathode mounted in the activation chamber and measured at the following stages:

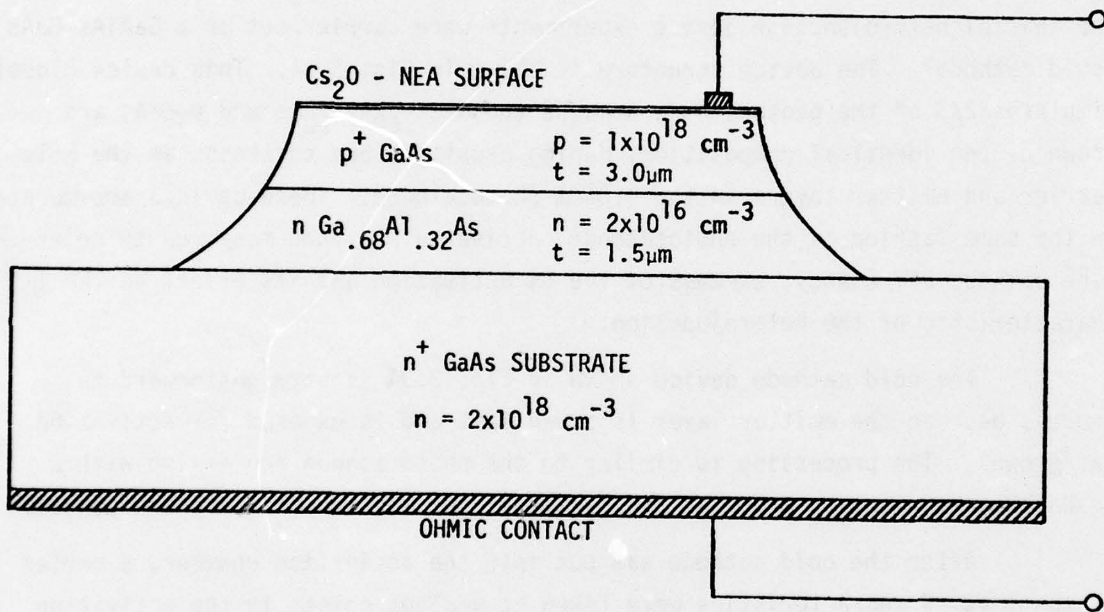

Fig. 3.34 **Schematic view of GaAs-GaAlAs heterojunction cold-cathode structure.**

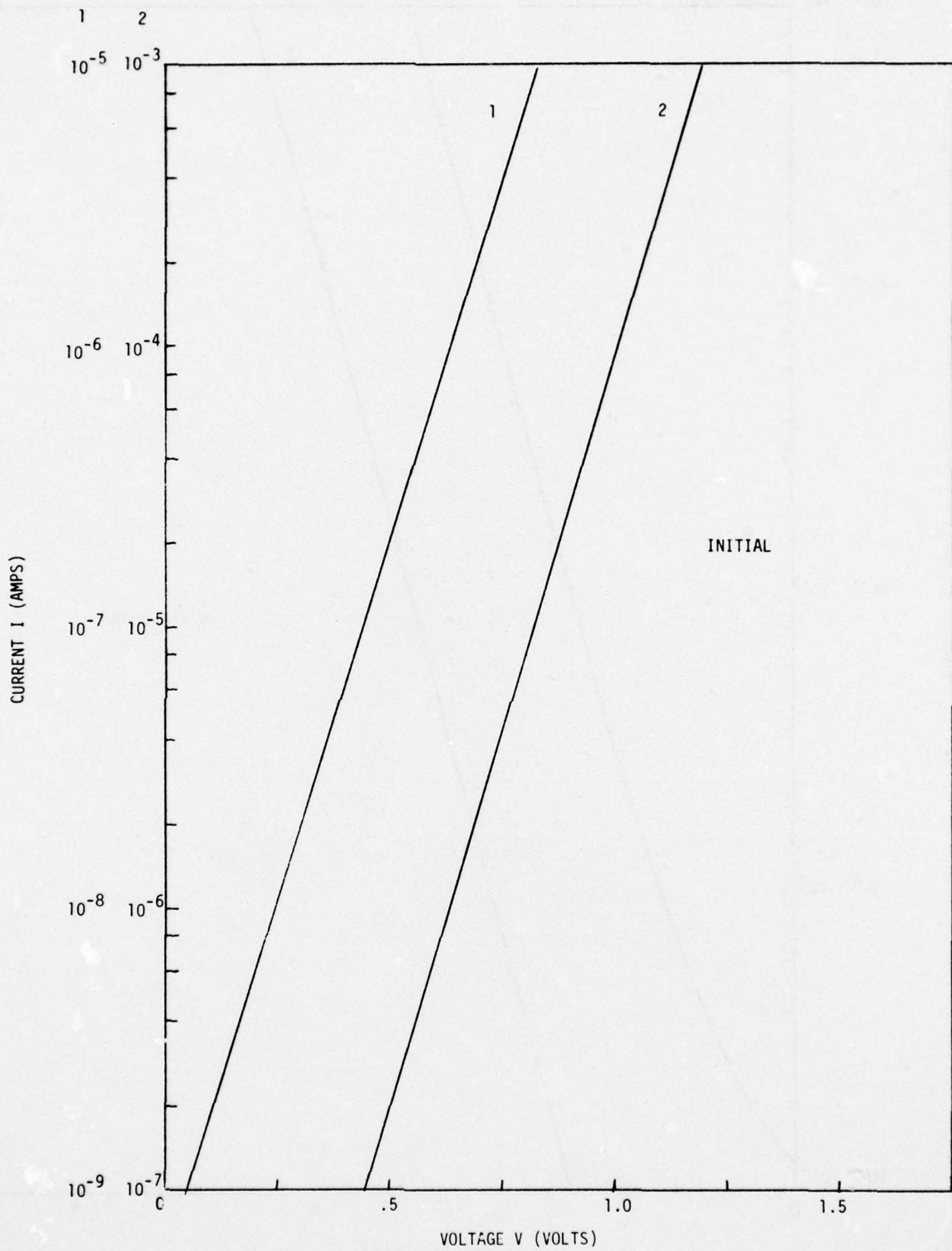

Fig. 3.35. Log I vs. V plots for a cold cathode sample mounted in the activation chamber before any processing.

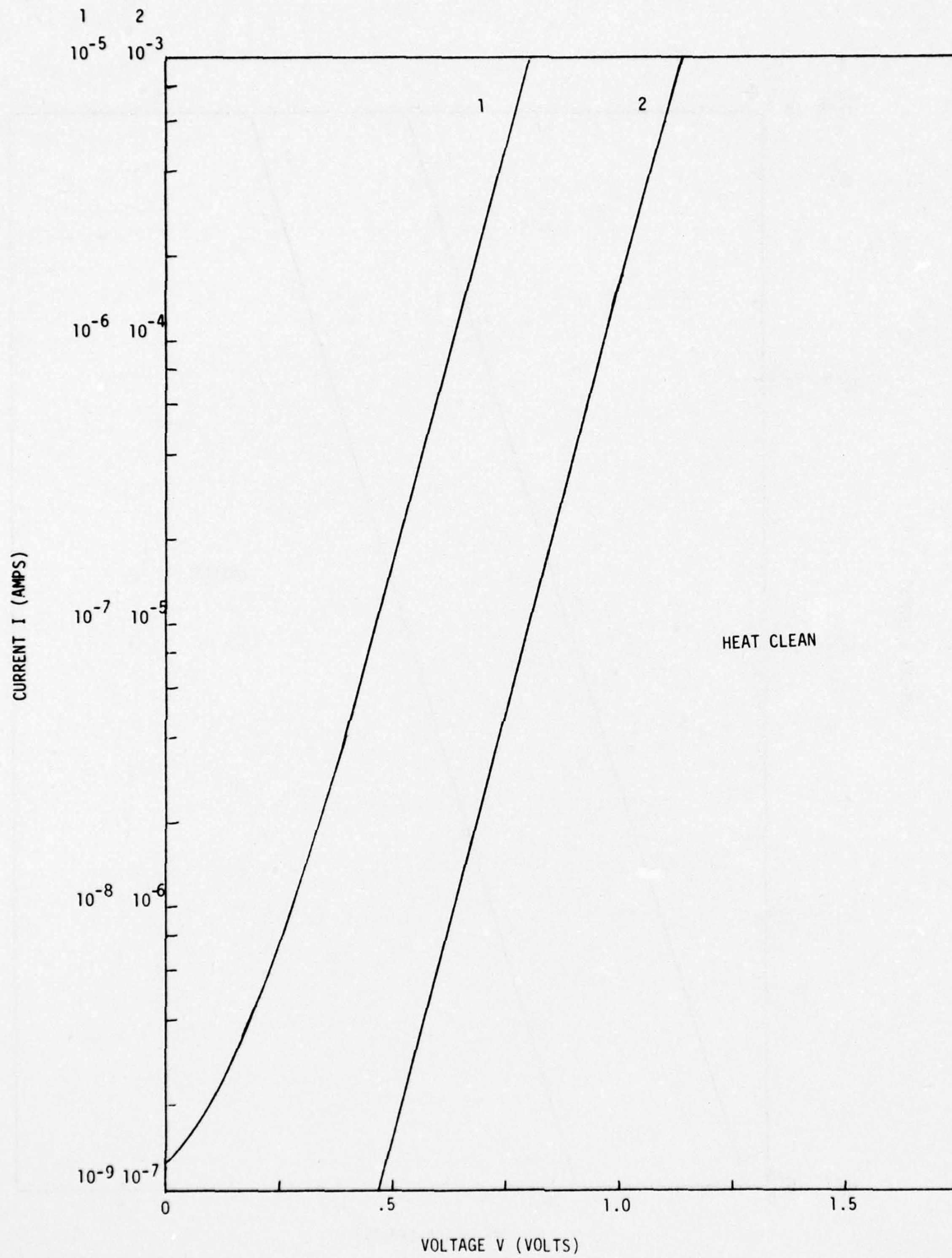

Fig. 3.36. Log I vs. V plots for the same cold cathode sample after heat cleaning for 2 min. at 610°C.

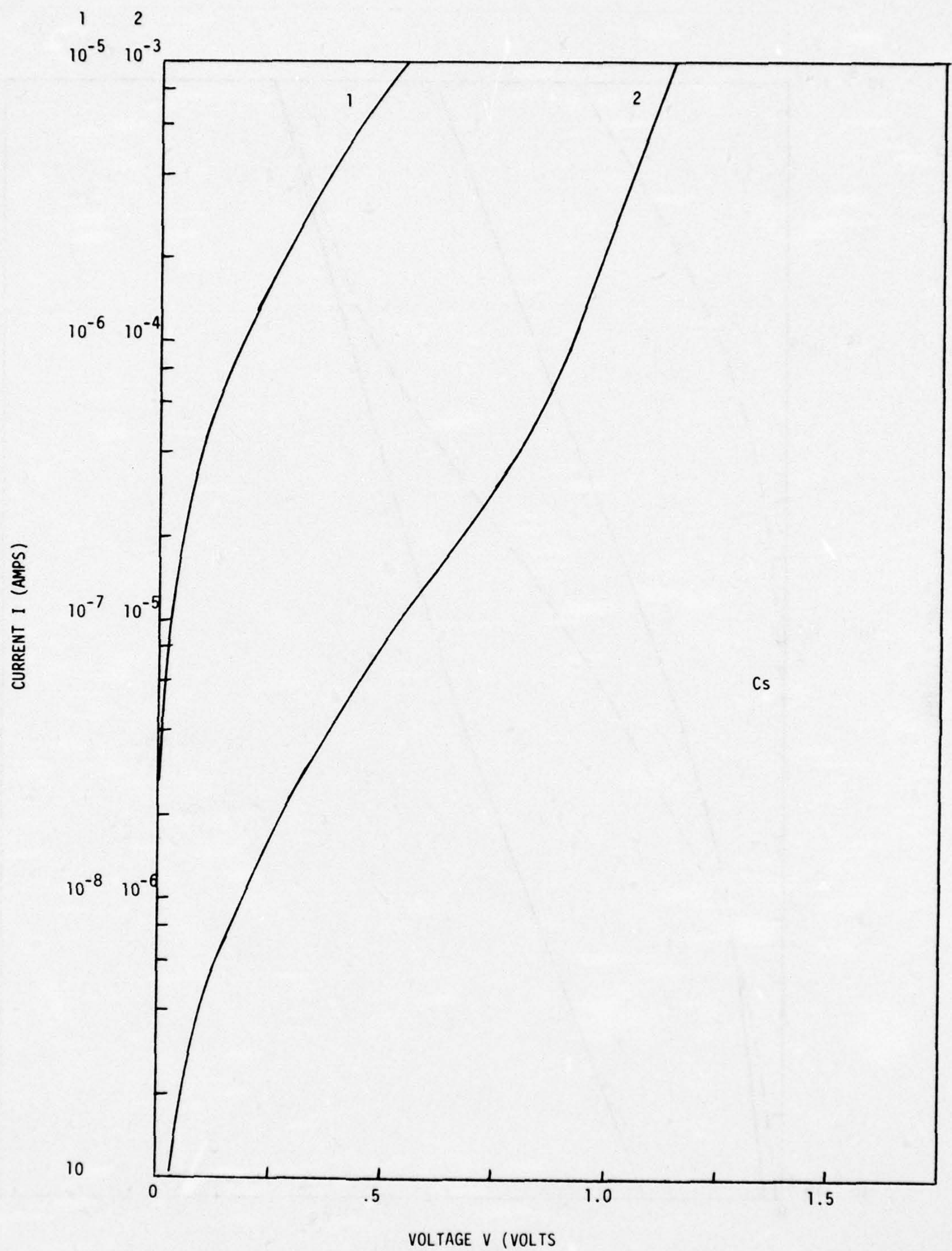

Fig. 3.37. Log I vs. V plots for the cold cathode sample after Cs and O_2 activation to reach NEA.

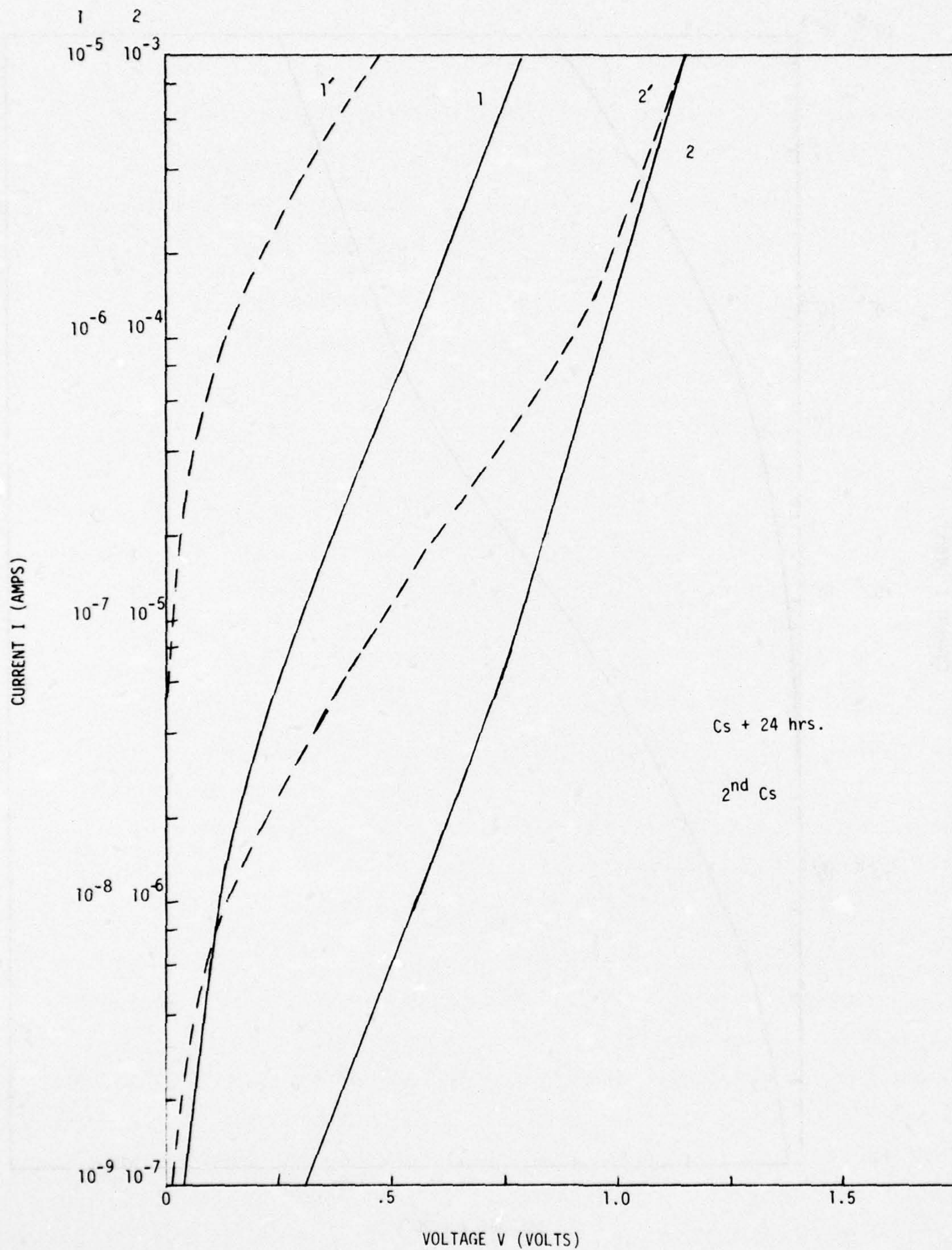

Fig. 3.38. Log I vs. V plots for the same cold cathode sample after allowing the sample to sit in the chamber for 24 hours (solid lines) and then after a second Cs and O_2 activation to achieve good photoemission (dashed lines).

a) Initial measurement, Fig. 3.35.

b) After heat cleaning to remove all of the O_2 from the surface, $\sim$ 610°C for two minutes, Fig. 3.36.

c) Application of alternate layers of Cs and O_2 to obtain maximum white light photoemission from the GaAs emitter, Fig. 3.37.

d) Allowing the device to sit 24 hours in a continuously pumped station (solid curves) and then reapplication of Cs and O_2 to peak the photoemission (dashed curves) Fig. 3.38.

The measurement in Fig. 3.36 clearly shows that the junction characteristic remains sound through the heat cleaning. This is not surprising since the devices are grown at 750°C. However, Fig.3.36 also shows that there is no change in the surface leakage current after heat cleaning. Fig. 3.37 reveals an enormous increase in current after the application of Cs_2O on the surface. At high current levels, the I-V characteristic in Fig. 3.37 is identical to that in Fig. 3.35, thus the junction current has not changed. The surface current has increased orders of magnitude due to a surface inversion region created by the Cs_2O layer on the mesa edge. Fig. 3.38 shows, however, that this surface region is not a permanent change because after 24 hours the I-V characteristic almost returns to the initial condition. This return of the I-V characteristic is accompanied by loss of the NEA surface condition and is consistent with Cs desorption from the surface.

In addition to these junction characteristics, cold cathode emission was measured from this device. The peak cold cathode emission efficiency was 0.01% at 50 ma forward bias junction current. A major factor in this low efficiency was the low escape probability of the GaAs surface ($\sim$ 0.01). The low escape probability is due to a high degree of C contamination on the surface which is not removed by heat cleaning. At the time these measurements were made, our sputtering techniques did not produce a good NEA surface (see 3.2.2.2 and Fig. 3.27), thus only heat cleaning was attempted which did not remove the C.

A second factor in the low device efficiency is that only a small fraction of the total device current results in electrons arriving at the emitter surface where they can be emitted into vacuum. This is due to: 1) current crowding near the contact region,[14] and 2) that a large fraction of the total current is g-r current in the depletion region rather than diffusion current resulting in the injection of electrons into the emitter. From the device geometry, the calculated junction current density across most of the device is ~ 20% of the average current density,[14] thus 80% of the current will be near or under the contacts with no chance for emission. This low emission measurement is not unexpected in light of the escape probability, device geometry and electron injection efficiency. These problems would all be greatly reduced by simply increasing the doping levels of both layers. This was not done because our goal was not to make an optimum cold cathode, but to simulate the HB-E portion of the photocathode and observe the effects of activation on this junction.

3.2.2.4 Double Heterojunction Photocathode Activation

Based upon our success in Cs activating GaAs surfaces (both heat cleaned and sputtered) and the GaAlAs-GaAs cold cathodes, we prepared several double heterojunction structures for activation. These devices were similar to that shown schematically in Fig. 3.24. The processing and fabrication of these devices was described in Section 3.2.1. After processing, the device was mounted onto a Mo plate with a W probe contacting the top emitter ohmic contact. The device was then given a final surface cleaning and inserted into the chamber.

The device was first heat cleaned at 590°C for 2 min. to remove all of the surface oxides. The Auger spectra of the emitter surface was similar to curve (a) in Fig. 3.33 except the C peak was about twice as large. This amount of C will decrease the electron escape probability, however, not enough to have any major effect on the device operation. We thus decided to Cs activate immediately rather than sputter clean the surface. The surface was activated in the manner described in Section 3.2.2.1 with an estimated reflec-

tive mode sensitivity of ~ 300μa/lumen (this value cannot be compared directly to a reflective mode device because the hole barrier-emitter p-n junction collects many of the photoelectrons generated in the emitter since the emitter layer is less than 1 electron diffusion length in thickness).

The I-V characteristic of the device was measured before and after activation and it was unchanged by the activation. The I-V characteristic after activation is shown in Fig. 3.39a). Measurement of the emitted current into vacuum revealed an immense increase with bias voltage, however, this emission turned out to be dark current and no photosensitive portion could be observed. At this point, our light source is not chopped, so that we are limited in picking up any small photoresponse that may have been buried by the high background dark current. While trying to study this dark current further, we encountered a problem with our Cs valve and excess Cs was admitted into the chamber. This excess Cs decreased the front surface photoemission from the GaAs, but in addition, it completely shorted out the photocathode device as shown by the I-V characteristic in Fig. 3.39b). This is most likely just a more dramatic effect of the Cs than that observed on the original cold cathodes described in the previous section. It is encouraging that the original activation without excess Cs did not effect the I-V characteristic and possibly one may avoid the mesa surface problems.

The results described here are from the very first double heterojunction structure to be completely fabricated and Cs activated. The dark current mechanism is not understood because we have not looked at more devices at this point. Such large dark currents were not observed in the internal photoemission measurements with the p-n junction collector structure,[1] and must be examined in detail to understand and eliminate them in the vacuum emission structure. This final result is encouraging because it demonstrates that our device processing, fabrication and Cs activation developments are nearing a point where they do not require major emphasis. We can now concentrate upon device measurements and characterization to optimize the structure in a continuing program to develop the double heterojunction photocathode.

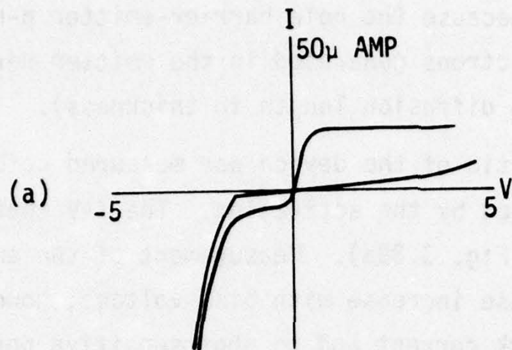

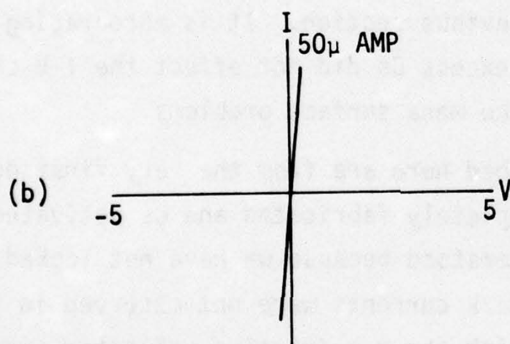

Fig. 3.39 Current vs. voltage characteristic for the double heterojunction photocathode. (a) Before and after cesiation, (remains identical) the 2 curves are in the dark and with white light on the emitter surface showing good collection of photoelectrons at the emitter-hole barrier junction. (b) After excess cesiation, the device becomes shorted.

Conclusions drawn from the heterojunction device activations are as follows:

1) Heterojunction devices, including the ohmic contacts, can withstand the heat cleaning temperatures required for Cs activation to achieve NEA.

2) Surface protection of exposed mesa surfaces will likely be required to eliminate the high surface leakage current created by the Cs application. This will probably not be required in order to demonstrate photocathode vacuum emission if excess cesiation is prevented. However, the surface problem will have to be solved to improve the device performance.

3) Sputter cleaning and thermal annealing will almost certainly be required on heterojunction devices because contact areas, mesas, etc. are photolithographically defined. Sputter cleaning may well be unnecessary in demonstrating photocathode emission, however, the device processing presently seems inconsistent with obtaining a C free, clean surface for optimum NEA activation.

4.0 CONCLUSIONS AND RECOMMENDATIONS

During the course of this program, significant progress was made in both the improvement of high sensitivity optical receivers and the development of field-assisted photocathodes.

In the optical receiver effort, a high sensitivity 5 MHz receiver was built utilizing a transimpedance type preamplifier. The performance of this receiver was better by a factor of 2 in a 1 MHz bandwidth than an equivalent Si avalanche photodiode receiver. A noise model was developed for the receiver including detailed noise sources from the avalanche photodiode and the input stage of the preamplifier. Based upon this model, considerably improved performance can be expected from this technology over that already achieved. In contrast, the Si APD receiver has now nearly reached its theoretical maximum performance.

The results of the GaAlSb APD work are still very preliminary. However, they look encouraging with respect to the depletion layer non-uniformity problems which presently limit the GaAsSb APD performance. The major advantage of the GaAlSb alloy system is that it is lattice matched and this appears to be an important requirement in improving APD performance.

We strongly recommend that the receiver work be continued to optimize the performance based upon the present measurements and noise model calculations. The major area which can now improve receiver performance is high avalanche gain APD's. Based upon our recent GaAlSb APD's, we recommend that this system or possibly GaInAsP on InP be pursued to achieve higher gain APD's.

In the field-assisted photocathode effort, state-of-the-art Cs activations on GaAs were achieved and sputter cleaning-annealing techniques were developed to produce good activations. A new heterojunction photocathode device structure was fabricated and the first double heterojunction device was successfully activated at the end of this program. No photoresponse or quantum efficiency measurements could be made because of the high dark current from the device when bias voltage was applied. At this point, we have no

concrete explanation for the excessive dark current, however, it appears that the unprotected mesa surfaces may be playing some role. Several more devices should be examined to determine the cause of the dark current.

The achievement of complete device fabrication and activation is a significant result and demonstrates that we are now approaching a device technology capable of producing the double heterojunction photocathode. We recommend that this double heterojunction photocathode effort be continued to understand and control or eliminate the dark current mechanisms in the device. Our progress to date is very encouraging and a continued research effort should yield the ultimate goal of a high sensitivity 1.06μm heterojunction photocathode.

5.0 REFERENCES

1. J. S. Harris and R. Sahai, "1.06 Micron High Sensitivity IR Photocathode," Technical Report #AFAL-TR-74-341.

2. J. S. Harris, R. Sahai, J. R. Waldrop and L. O. Bubulac, "1.06 Micron High Sensitivity IR Photocathode," Technical Report #AFAL-TR-76- .

3. R. C. Eden, "1.06 Micrometer Avalanche Photodiode Detector," Technical Report #AFAL-TR-76- .

4. I. Deyhimy, K. Nakano and R. C. Eden, "1.06 Micrometer APD/Low Noise Preamplifier," Technical Report #AFAL-TR-76- .

5. J. S. Harris and S. J. Anderson, "Photocathode Study at 1.8 Microns," Semi-Annual Technical Reports on Contract #DAAK02-73-C-0231.

6. I. I. Burdian, Sov. Phys. Solid State 1, 246 (1960).

7. J. F. Miller, H.L. Goering and R. C. Himes, H. Electrochem. Soc. 107, 527 (1960).

8. K. Y. Cheng, "Preparation and Properties of $Al_xGa_{1-x}Sb$ for Application to Luminescent Devices," PhD Thesis, Stanford University, 1975. Stanford Electronics Laboratory Technical Report #5111-5, Aug. 1975.

9. D. Eastman, private communication.

10. T. Pearsall, R. E. Nahory and M. A. Pollack, Appl. Phys. Lett. 27, 330 (1975).

11. H. Olsen and M. Ettenberg, J. Appl. Phys. 45, 5172 (1974).

12. R. L. Bell, Negative Electron Affinity Devices, (Clarendon Press, Oxford, 1973).

13. S. Sze, Physics of Semiconductor Devices, (John Wiley, New York, 1969).

14. Elliott Kohn, J. Appl. Phys. 42, 2493 (1971).

☆ U. S. GOVERNMENT PRINTING OFFICE: 1976 — 757-001/99